Monthly Notices
of the
ROYAL ASTRONOMICAL SOCIETY

MNRAS **503,** 2349–2368 (2021)
Advance Access publication 2021 February 26

doi:10.1093/mnras/stab528

Infrared emission of $z \sim 6$ galaxies: AGN imprints

F. Di Mascia,[1]★ S. Gallerani,[1] C. Behrens,[2] A. Pallottini,[1] S. Carniani,[1] A. Ferrara,[1] P. Barai,[3,4] F. Vito[1] and T. Zana[1]

[1]*Scuola Normale Superiore, Piazza dei Cavalieri 7, I-56126 Pisa, Italy*
[2]*Institut für Astrophysik, Georg-August Universität Göttingen, Friedrich-Hundt-Platz 1, D-37077, Göttingen, Germany*
[3]*Núcleo de Astrofísica - Universidade Cidade de São Paulo, Rua Cesário Galeno 448, São Paulo, 03071-000, Brazil*
[4]*Universidade Cruzeiro do Sul, Rua Galvão Bueno 868, São Paulo 01506-000, Brasil*

Accepted 2021 February 16. Received 2021 February 16; in original form 2020 October 1

ABSTRACT

We investigate the infrared (IR) emission of high-redshift ($z \sim 6$), highly star-forming (SFR $> 100\,M_\odot\,yr^{-1}$) galaxies, with/without active galactic nuclei (AGN), using a suite of cosmological simulations featuring dust radiative transfer. Synthetic spectral energy distributions (SEDs) are used to quantify the relative contribution of stars/AGN to dust heating. In dusty ($M_d \gtrsim 3 \times 10^7\,M_\odot$) galaxies, $\gtrsim$50–90 per cent of the ultraviolet (UV) radiation is obscured by dust inhomogeneities on scales $\gtrsim$100 pc. In runs with AGN, a clumpy, warm ($\approx$250 K) dust component coexists with a colder ($\approx$60 K) and more diffuse one, heated by stars. Warm dust provides up to 50 per cent of the total infrared (IR) luminosity, but only $\lesssim$0.1 per cent of the total mass content. The AGN boosts the MIR flux by 10–100 times with respect to star-forming galaxies, without significantly affecting the far-IR. Our simulations successfully reproduce the observed SED of bright ($M_{UV} \sim -26$) $z \sim 6$ quasars, and show that these objects are part of complex, dust-rich merging systems, containing multiple sources (accreting black holes and/or star-forming galaxies) in agreement with recent *HST* and ALMA observations. Our results show that the proposed ORIGINS missions will be able to investigate the mid-IR (MIR) properties of dusty star-forming galaxies and to obtain good-quality spectra of bright quasars at $z \sim 6$. Finally, the MIR-to-FIR flux ratio of faint ($M_{UV} \sim -24$) AGN is >10 times higher than for normal star-forming galaxies. This implies that combined *JWST*/ORIGINS/ALMA observations will be crucial to identify faint and/or dust-obscured AGN in the distant Universe.

Key words: methods: numerical – galaxies: evolution – galaxies: high-redshift – galaxies: ISM – quasars: supermassive black holes – infrared: general.

1 INTRODUCTION

Gas accretion on to supermassive black holes (SMBHs, $M_{BH} \sim 10^6-10^{10}\,M_\odot$) residing in the centre of most massive galaxies ($M_\star \sim 10^9-10^{12}\,M_\odot$; e.g. Kormendy & Richstone 1995; Magorrian et al. 1998; Marconi et al. 2004; Kormendy & Ho 2013) turns them into active galactic nuclei (AGN). A large fraction (∼10–50 per cent) of the bolometric luminosity produced by accreting BHs is emitted into optical/ultraviolet (UV) wavelength range (Hopkins, Richards & Hernquist 2007; Lusso et al. 2015; Shen et al. 2020), adding up to the luminosity produced by massive OB stars. Thus, rest-frame optical/UV bands [redshifted in the near-infrared (NIR) for objects located in the Epoch of Reionization (EoR)] represent the natural spectral windows for AGN searches.

Over the last decade, thanks to several optical/NIR surveys, such as the Sloan Digital Sky Survey (SDSS; Fan et al. 2006; Jiang et al. 2009), the UKIDSS Large Area Survey (Venemans et al. 2007), the Canada–France High-z Quasar Survey (Willott et al. 2007), the VISTA Kilo-Degree Infrared Galaxy Survey (Venemans et al. 2013, 2015), Pan-STARRS1 (Bañados et al. 2014), the Very Large Telescope Survey Telescope ATLAS survey (Carnall et al. 2015), the Dark Energy Survey (Reed et al. 2015, and the Subaru High-z Exploration of Low-luminosity Quasars (Kashikawa et al. 2015; Matsuoka et al. 2016), more than 200 quasars have been discovered at the most distant redshifts probed so far ($z \sim 6-8$, Mortlock et al. 2011; Bañados et al. 2018; Wang et al. 2018, 2021). Follow-up NIR spectroscopical observations of emission lines (e.g. Mg II and C IV) produced by broad-line region clouds have confirmed that these sources are powered by $\sim 10^8-10^{10}\,M_\odot$ BHs (Fan et al. 2000; Willott, McLure & Jarvis 2003; Jiang et al. 2007; Kurk et al. 2007; Wu et al. 2015). The challenge is to understand how SMBHs have formed in <1 Gyr, namely the age of the Universe at $z \sim 6$. Theoretical models of black hole (BH) accretion are in fact facing serious difficulties in explaining such a rapid growth (e.g. Volonteri, Haardt & Madau 2003; Tanaka & Haiman 2009; Haiman 2013; Pacucci, Volonteri & Ferrara 2015; Lupi et al. 2016), also including the rather uncertain formation mechanism of SMBH seeds (Shang, Bryan & Haiman 2010; Latif et al. 2013; Schleicher et al. 2013; Ferrara et al. 2014; Latif & Ferrara 2016).

The problem is exacerbated by the unsuccessful search for high-z AGN powered by $\sim 10^6-10^7\,M_\odot$ BHs (e.g. Xue et al. 2011; Cowie et al. 2020). Whether these sources are too rare (Pezzulli et al. 2017), and/or too faint to be detected by current optical/NIR survey (Willott

★ E-mail: fabio.dimascia@sns.it

et al. 2010; Jiang et al. 2016; Pacucci et al. 2016; Matsuoka et al. 2018; McGreer et al. 2018; Kulkarni, Worseck & Hennawi 2019; Wang et al. 2019), and/or their optical/UV emission is obscured by dust, remains unclear. This latter hypothesis is supported by at least two observational results: (i) multiwavelength studies of ∼1000 local AGN show a decrease in the covering factor of the circumnuclear material with increasing accretion rates due to the increase of the dust sublimation radius of the obscuring material with incident luminosity (e.g. Ricci et al. 2017); (ii) X-ray observations provide indications that the fraction of obscured AGN increases with redshift (e.g. Vito et al. 2014, 2018), evidence further supported by studies of Lyα absorption profiles of distant quasars (e.g. Davies, Hennawi & Eilers 2019). Both these facts resonate with the expectation that early growth of SMBHs, typically characterized by low accretion rates, is buried in a thick cocoon of dust and gas (e.g. Hickox & Alexander 2018, for a review on this subject).

In this scenario, a certain fraction of UV photons are absorbed and/or scattered by dust grains in gas clouds in the host galaxy. By transferring energy and momentum to the surrounding dusty environment, AGN radiation can substantially affect the conditions of the interstellar medium (ISM) and circumgalactic (CGM) medium of the host galaxy in several ways. UV radiation heats the dust, leading grains to re-emit in the far-IR. Moreover, radiation pressure on dust grains may drive powerful outflows (e.g. Fabian 1999; Murray, Quataert & Thompson 2005; Wada, Schartmann & Meijerink 2016; Venanzi, Hönig & Williamson 2020) that push away the gas surrounding the BH, clean up the line of sight, and prevent further accretion on to the BH (Di Matteo, Springel & Hernquist 2005; Sijacki et al. 2007; Barai et al. 2018). In addition to that, it is unclear whether star formation in the host galaxy might be quenched (Schawinski et al. 2006; Dubois et al. 2010, 2013; Teyssier et al. 2011; Schaye et al. 2015; Weinberger et al. 2018) or triggered (De Young 1989; Silk 2005; Zinn et al. 2013; Zubovas et al. 2013; Cresci et al. 2015a,b; Carniani et al. 2016) by AGN-driven outflows.

Signatures of such a complex interplay between AGN/stellar radiation and dust grains remain imprinted in the rest-frame UV-to-FIR spectral energy distribution (SED) of galaxies. Therefore, multiwavelength SED analysis of galaxies and AGN can be used to infer information on their dust properties (mass, temperature, grain size distribution, and composition), to shed light on their star formation and nuclear activities, and to quantify the relative contribution of stars and AGN radiation to dust heating (Bongiorno et al. 2012; Pozzi et al. 2012; Berta et al. 2013; Gruppioni et al. 2016). Telescopes sensitive to Mid-IR (MIR, $5 \lesssim \lambda_{RF} \lesssim 40\,\mu$m), like *Spitzer* (Werner et al. 2004) and *Herschel* (Pilbratt et al. 2010), and to FIR ($45 \lesssim \lambda_{RF} \lesssim 350\,\mu$m) wavelengths (e.g. ALMA, NOEMA) have made possible to study the panchromatic SED of bright ($M_{UV} \lesssim -26$) quasars at $z \sim 6$.

SEDs observations obtained with *Herschel* and *Spitzer* in these sources (Leipski et al. 2013, 2014) have been used to disentangle the star formation versus AGN contribution to the total rest-frame IR emission (total IR, TIR, $8 < \lambda_{RF} < 1000\,\mu$m). The result of this study is that star formation may contribute 25−60 per cent to the bolometric TIR luminosity, with strong variations from source to source. In particular, Leipski et al. (2014) performed a multicomponent SED analysis on a sample of 69 $z > 5$ quasars, finding that a clumpy torus model needs to be complemented by a hot (∼1300 K) dust component to match the NIR data, and by a cold (∼50 K) dust component for the FIR emission. This work shows that, in addition to the standard AGN-heated component, a large variety of dust conditions is required to reproduce the observed SED. Yet these kinds of studies are limited to a small sample of bright sources. Future facilities in the rest-frame MIR, such as the proposed Origins Space Telescope (OST; Wiedner et al. 2020) with a sensitivity ∼1000 higher than its precursors *Spitzer* and *Herschel*, will significantly improve our knowledge of dusty galaxies in the EoR.

ALMA and NOEMA observations have provided the opportunity of studying the ISM/CGM properties of bright $z \sim 6$ quasar hosts (e.g. Carilli & Walter 2013; Gallerani et al. 2017a), by means of rest-frame FIR emission lines, as the [C II] line at 158 micron (e.g. Maiolino et al. 2005; Walter et al. 2009; Wang et al. 2013; Venemans et al. 2016; Novak et al. 2019), CO rotational transitions (e.g. Walter et al. 2003; Bertoldi et al. 2003b; Riechers et al. 2009; Gallerani et al. 2014; Venemans et al. 2017a; Carniani et al. 2019; Li et al. 2020), and the corresponding dust continuum emission (e.g. Bertoldi et al. 2003a; Venemans et al. 2016, 2017b; Novak et al. 2019). These observations have shown that these massive galaxies ($M_{dyn} \sim 10^{10}-10^{11}\,M_\odot$) are characterized by high star formation rates (SFRs) (SFR ∼ 100–1000 $M_\odot\,yr^{-1}$), and large amount of molecular gas ($\sim 10^{10}\,M_\odot$) and dust ($\sim 10^{8}\,M_\odot$), that are typically distributed on galactic scales ($\lesssim$5 kpc). In some exceptional cases (Maiolino et al. 2012; Cicone et al. 2015), the extension of [C II] emitting gas has been detected up to CGM scales (∼20–30 kpc), possibly driven by fast-outflowing gas ($v_{out} \gtrsim 1000\,km\,s^{-1}$) with extreme mass outflow rate of $\dot{M}_{out} \sim 1000\,M_\odot\,yr^{-1}$.

These FIR data, combined with X-ray, and UV observations, have shown the presence of galaxy/AGN companions in the field of $z \sim 6$ quasars. In the X-ray, whereas the fraction of dual AGN can be as high as ∼40–50 per cent out to $z \sim 4.5$ (e.g. Koss et al. 2012; Vignali et al. 2018; Silverman et al. 2020), at $z \sim 6$, there are only tentative X-ray detections of double systems (e.g. Vito et al. 2019b; Connor et al. 2019, but see also Connor et al. 2020.)

The occurrence of UV detected and sub-mm galaxy (SMG) companions is instead more frequent: Marshall et al. (2020) detected up to nine companions with $-22 \lesssim M_{UV} \lesssim -20$ in the field of view of six quasars at $z \sim 6$ (but see also Mechtley et al. 2012); Decarli et al. (2017) reported the [C II] line and 1-mm continuum (F_{cont}) detection of SMGs close to 4 (out of ∼20) quasars at $z \sim 6$, with $0.2 \lesssim F_{cont} \lesssim 2.0$ mJy, and reported projected distances between ∼8 and ∼60 kpc.

ALMA data of $z \sim 8$ Lyman Break Galaxies (LBGs; Laporte et al. 2017; Bakx et al. 2020) have suggested the presence in these sources of dust hotter than expected ($T \sim 60$–$90\,K$, Behrens et al. 2018; Arata et al. 2019; Sommovigo et al. 2020). The origin of warm dust in early galaxies can be traced back to their (i) large SFR surface densities that favour an efficient heating of dust grains (Behrens et al. 2018) and (ii) more compact structure of molecular clouds (MC) that delays their dispersal by stellar feedback, implying that a large fraction (∼40 per cent) of the total UV radiation remains obscured (Sommovigo et al. 2020). Another possibility concerns the presence of obscured, accreting, massive ($\sim 10^{8}\,M_\odot$) BHs, whose UV luminosity is absorbed by dust located in the ISM of the host ($\lesssim$1 kpc) and/or into a central obscurer, closer to the active nuclei (∼1 pc), and heated to temperatures as high as 80–500 K, respectively (Orofino et al. 2021). According to this scenario, buried AGN should be searched for among LBGs populating the bright-end of their UV luminosity function ($-24 < M_{UV} < -22$), where indeed a large fraction of objects consists of spectroscopically confirmed AGN (Ono et al. 2018).

Obscured AGN may therefore represent a bridge between LBGs and bright quasars in the galaxy formation process. In this appealing scenario, the following questions arise: *(i) If high-z galaxies contain*

an obscured AGN, does this imply warmer dust temperatures? (ii) Is there a relation between the dust temperature and the BH accretion rate? (iii) What are the most promising spectral ranges and observational strategies to detect obscured AGN? To answer these questions, it is necessary to build up a model that follows the coevolution of BHs with their host galaxy from their birth up to the formation of SMBHs powering $z \sim 6$ quasars, while accounting for AGN and stellar feedback. The final aim is to produce synthetic multiwavelength SEDs that can be directly compared with the aforementioned observations of $z \sim 6$ quasars to validate the underlying galaxy-BH formation model. This can be done by post-processing cosmological hydrodynamical simulations with dust radiative transfer (RT) calculations.

Several works in the past years made use of RT simulations to understand the AGN contribution to the total IR emission of a galaxy, mainly focusing on ultraluminous infrared galaxies, and late-stage mergers (e.g. Chakrabarti et al. 2007; Chakrabarti & Whitney 2009; Younger et al. 2009; Snyder et al. 2013; Roebuck et al. 2016; Blecha et al. 2018). However, these studies are limited up to $z \sim 3$ and they rely on hydrodynamical simulations in which the ICs of both the DM and gas components were set with analytical prescriptions. Recently, Schneider et al. (2015) have studied the origin of the infrared emission in SDSS J1148+5251, a $z \sim 6$ quasar, by applying dust RT calculations to the output of a semi-analytical merger tree code finding that the dust heating by the AGN radiation may contribute up to 70 per cent of the total IR luminosity. This is consistent with the results found by Li et al. (2008) that computed RT calculations on hydrodynamical simulations of luminous quasars to reproduce the SED of SDSS J1148+5251. They also found that the AGN contribution to the IR emission is significant, because dust heating is dominated by the central source during the quasar-phase.

In this work, we investigate the imprints of AGN in the IR emission of $z \sim 6$ galaxies by post-processing cosmological hydrodynamic simulations of SMBHs formation (Barai et al. 2018, hereafter B18) with dust RT calculations performed by using the code SKIRT. The B18 simulations studied the growth of SMBHs (10^8-10^9 $M_\odot$ at $z = 6$) and the impact of different AGN feedback prescriptions on their host galaxies, residing in an $\sim 10^{12}$ $M_\odot$ DM halo.

The paper is organized as follows: In Section 2, we illustrate both the hydrodynamical simulations (Section 2.1) and the model adopted for the RT calculations (Section 2.2). We present our results in Section 3 and we compare them with observations in Section 4. We then make predictions for the proposed mission ORIGINS in Section 5. Finally, we summarize our results in Section 6 along with our conclusions.

2 NUMERICAL MODEL

We describe the main characteristics of the hydrodyamical simulations adopted in this work in Section 2.1 and we present the RT post-processing analysis runs performed in Section 2.2, where we also discuss the details of the numerical setup and the assumptions made for the dust properties and emitting sources.

2.1 Hydrodynamical simulations

The hydrodynamical cosmological zoom-in simulations used in this work are described in details in B18 and we summarize the main points in the following.

B18 use a modified version of the smooth particle hydrodynamics (SPH) N-body code GADGET-3 (Springel 2005) to follow the evolution of a comoving volume of $(500\,\mathrm{Mpc})^3$, starting from cosmological initial condition (IC)[1] generated with MUSIC (Hahn & Abel 2011) at $z = 100$ and zooming-in on the most massive dark matter (DM) halo inside the box down to $z = 6$.[2] The mass resolution is $m_{\rm DM} = 7.54 \times 10^6\,M_\odot$ and $m_{\rm gas} = 1.41 \times 10^6\,M_\odot$ for DM and gas particles, respectively. For these high-resolution DM and gas particles, the gravitational softening length is 1 h^{-1} kpc comoving. For the gas, the smoothing length is determined at each time-step according to the local density and typically ranges from 300 pc in the ISM ($n \approx 100\,\mathrm{cm^{-3}}$) to 6.5 kpc in the CGM ($n \approx 10^{-2}\,\mathrm{cm^{-3}}$).

The code accounts for radiative heating and cooling according to the tables computed by Wiersma, Schaye & Smith (2009), which also include metal-line cooling. Star formation in the ISM is implemented following the multiphase model by Springel & Hernquist (2003), adopting a density threshold for star formation of $n_{\rm SF} = 0.13\,\mathrm{cm^{-3}}$ and a Chabrier (2003) initial mass function (IMF) in the mass range 0.1–100 $M_\odot$. Stellar evolution and chemical enrichment are computed for the 11 element species (H, He, C, Ca, O, N, Ne, Mg, S, Si, and Fe) tracked in the simulation, following Tornatore et al. (2007). Kinetic feedback from supernovae (SN) is included by relating the wind mass-loss rate ($\dot{M}_{\rm SN}$) with the SFR ($\dot{M}_\star$) as $\dot{M}_{\rm SN} = \eta \dot{M}_\star$ and assuming a mass-loading factor $\eta = 2$. The wind kinetic energy is set to a fixed fraction χ of the the SN energy: $\frac{1}{2}\dot{M}_{\rm SN} v_{\rm SN}^2 = \chi \epsilon_{\rm SN} \dot{M}_\star$, where $v_{\rm SN} = 350\,\mathrm{km\,s^{-1}}$ is the wind velocity and $\epsilon_{\rm SN} = 1.1 \times 10^{49}$ erg $M_\odot^{-1}$ is the average energy released by an SN for each $M_\odot$ of stars formed.[3]

In the simulation, each BH is treated as a collisionless sink particle and the following seeding prescription is used. When a DM halo – that is not already hosting a BH – reaches a total mass of $M_{\rm h} = 10^9\,M_\odot$, an $M_{\rm BH} = 10^5\,M_\odot$ BH is seeded at its gravitational potential minimum location. BHs are allowed to grow by accretion of the surrounding gas or by mergers with other BHs. Gas accretion on to the BH is modelled via the classical Bondi–Hoyle–Littleton accretion rate $\dot{M}_{\rm Bondi}$ (Hoyle & Lyttleton 1939; Bondi & Hoyle 1944; Bondi 1952) and it is capped at the Eddington rate $\dot{M}_{\rm Edd}$. The final BH accretion rate $\dot{M}_{\rm BH}$ reads as follows:

$$\dot{M}_{\rm BH} = \min(\dot{M}_{\rm Bondi}, \dot{M}_{\rm Edd}). \quad (1)$$

To avoid BHs moving from the centre of the halo in which they reside because of numerical spurious effects, we implement BH repositioning or *pinning* (see also e.g. Springel, Di Matteo & Hernquist 2005; Sijacki et al. 2007; Booth & Schaye 2009; Schaye et al. 2015): At each time-step BHs are shifted towards the position of minimum gravitational potential within their softening length. During its growth, a BH radiates away a fraction of the accreted rest-mass energy, with a bolometric luminosity

$$L_{\rm bol} = \epsilon_{\rm r} \dot{M}_{\rm BH} c^2, \quad (2)$$

where c is the speed of light and $\epsilon_{\rm r}$ is the radiative efficiency. B18 set

[1] A flat ΛCDM model is assumed with the following cosmological parameters (Planck Collaboration XIII 2016): $\Omega_{\rm M,0} = 0.3089$, $\Omega_{\Lambda,0} = 0.6911$, $\Omega_{\rm B,0} = 0.0486$, and $H_0 = 67.74\,\mathrm{km\,s^{-1}\,Mpc^{-1}}$.

[2] In the low-resolution DM-only simulation, the most massive halo at $z = 6$ has a mass of $M_{\rm halo} = 4.4 \times 10^{12}\,M_\odot$ (virial radius $R_{200} = 511$ kpc comoving), massive enough to host luminous AGN, as suggested by clustering studies (e.g. Allevato et al. 2016).

[3] In the ISM multiphase model adopted here (Springel & Hernquist 2003), kicked particles mimicking stellar winds are temporarily hydrodynamically decoupled. This procedure may affect both the properties of the resulting outflows and the structure of the surrounding ISM (e.g. Dalla Vecchia & Schaye 2008).

Table 1. Summary of the hydrodynamic runs of B18 used in this work. For each run, we indicate the feedback model used in the simulation and the main physical properties of the zoomed-in halo at $z = 6.3$ within a cubic region of 60 kpc size (that corresponds to ∼50 per cent of the virial radius): gas mass ($M_{\rm gas}$), stellar mass ($M_\star$), SFR (averaged over the last 10 Myr), and the sum of the accretion rate of all the BHs in the selected region ($\dot{M}_{\rm BH}$). We further associate to $\dot{M}_{\rm BH}$ an intrinsic UV magnitude $M_{\rm UV}$ (see Appendix C).

Simulation run	AGN feedback	$M_{\rm gas}$ ($\rm M_\odot$)	$M_\star$ ($\rm M_\odot$)	SFR ($\rm M_\odot\,yr^{-1}$)	$\dot{M}_{\rm BH}$ ($\rm M_\odot\,yr^{-1}$)	$M_{\rm UV}$ (mag)
noAGN	No	2.9×10^{11}	1.2×10^{11}	600	–	
AGNsphere	Spherical	2.1×10^{11}	6.5×10^{10}	312	3.1	−24.32
AGNcone	Bi-conical	1.4×10^{11}	7.0×10^{10}	189	89	−27.97

$\epsilon_{\rm r} = 0.1$, a fiducial value for radiatively efficient, geometrically thin, optically thick accretion discs around a Schwarzschild BH (Shakura & Sunyaev 1973). A fraction $\epsilon_{\rm f} = 0.05$ of this energy is distributed to the surrounding gas in a kinetic form.[4]

In this work, we consider the following three runs performed by B18, starting from the same ICs:

(i) *noAGN*: Control simulation without BHs.

(ii) *AGNsphere*: Simulation accounting for BH accretion and AGN feedback. The kinetic feedback is distributed according to a spherical geometry.

(iii) *AGNcone*: Same as the *AGNsphere* run, but with kinetic feedback distributed inside a bi-cone with a half-opening angle of 45°.

In Table 1, we report the main physical properties of the zoomed-in halo at $z = 6.3$ inside a cubic region of 60 physical kpc size (the virial radius of the most massive halo is ≈60 kpc) centred on the halo's centre of mass. This choice allows to have an overview of all the relevant dynamical structures around the central galaxy, i.e. satellites, clumps, filaments, and star-forming regions.

In Fig. 1, we show the hydrogen column density (top row) and the SFR (middle row) for the zoomed-in halo in the three simulations for a line of sight aligned with the angular momentum of the particles inside the selected region. In the following, this is our reference line of sight. From the top row, it can be seen that the central region, corresponding to the main galaxy, is characterized by the highest column density in all the runs. It reaches values of $N_{\rm H} \sim 6 \times 10^{24}$ cm^{-2} in the *noAGN* run, whereas it is an order of magnitude lower when AGN feedback is included. This is because kinetic feedback kicks gas away from the accreting BHs. In turn, the decreased gas density quenches the overall SFR density. In fact, SFR densities $\Sigma_{\rm SFR}$ as high as $\Sigma_{\rm SFR} \approx 600\,\rm M_\odot\,yr^{-1}\,kpc^{-2}$ are found in the *noAGN* run, in sharp contrast with those in the *AGNsphere* ($\approx 130\,\rm M_\odot\,yr^{-1}\,kpc^{-2}$, characterized by a total BH accretion rate $\dot{M}_{\rm BH} = 3.1\,\rm M_\odot\,yr^{-1}$), and *AGNcone* ($\approx 50\,\rm M_\odot\,yr^{-1}\,kpc^{-2}$, $\dot{M}_{\rm BH} = 89\,\rm M_\odot\,yr^{-1}$) cases. The same trend is observed also for the total SFR, as reported in Table 1.

2.2 Radiative transfer

We post-process the snapshots at $z = 6.3$ of the three selected hydrodynamic simulations in B18 by using the publicly available code SKIRT[5] (Baes et al. 2003; Baes & Camps 2015; Camps & Baes 2015; Camps et al. 2016). SKIRT solves the continuum RT problem in a dusty medium with a Monte Carlo approach, by sampling the SED of the sources with a finite number of photon packets (in the following simply referred to as *photons*). Photons are scattered and/or absorbed by dust grains in the simulation volume according to their properties. Dust grains, after being heated up, thermally re-emit the absorbed energy at IR wavelengths. One of the main advantages of the SKIRT code is its flexibility: It allows the user to handle input data from different numerical codes (e.g. Adaptive Mesh Refinement and SPH codes), to account for different dust properties (i.e. grain-size distribution and composition), to implement different SEDs for the radiating sources (e.g. stars and accreting BHs), to include many physical mechanisms (e.g. dust stochastic heating and self-absorption).

To relate the energy absorbed by dust with its wavelength-dependent emissivity, we adopt the dust models described in Section 2.2.1. We describe the SED adopted in different RT runs for stars and accreting BHs in Section 2.2.3.

2.2.1 Dust properties

Dust formation, growth, and destruction processes are not tracked in the hydrodynamic simulations considered here. Similarly to other RT works (Behrens et al. 2018; Arata et al. 2019; Liang et al. 2019), we derive the dust mass distribution by assuming a linear scaling with the gas metallicity[6] (Draine et al. 2007), parametrizing the mass fraction of metals locked into dust as

$$f_d = M_{\rm d}/M_Z, \tag{3}$$

where $M_{\rm d}$ is the dust mass and M_Z is the total mass of all the metals in each gas particle in the hydrodynamical simulation (see Section 2.1). The choice of $f_{\rm d}$ directly affects the total dust content. The RT calculation is sensitive to the $f_{\rm d}$ value, which is poorly constrained by high-redshift galaxies observations (see Wiseman et al. 2017, and references therein) and theoretical models (Nozawa et al. 2015). In particular, recent theoretical works (Asano et al. 2013a; Aoyama et al. 2017) suggest that $f_{\rm d}$ is constant in the early stages of galaxy evolution and then it grows with metallicity up to the Milky Way (MW) value of $f_{\rm d} = 0.3$ when/if dust growth becomes important. However, the efficiency of dust growth in the ISM of early galaxies is highly debated (Ferrara, Viti & Ceccarelli 2016). In this work, we consider a constant value of $f_{\rm d}$, and focus our attention on how the dust content of galaxies affects their panchromatic SED.

We adopt two different $f_{\rm d}$ values for the normalization: (i) an MW like value ($f_{\rm d} = 0.3$); (ii) a lower value ($f_{\rm d} = 0.08$) tuned for hydrosimulations (Pallottini et al. 2017; Behrens et al. 2018) to reproduce the observed SED of a $z \sim 8$ galaxy (Laporte et al. 2017).

[4]We refer to B18 for details about the choice of the value for $\epsilon_{\rm f}$ and the numerical implementation of the kinetic feedback.

[5]Version 8, http://www.skirt.ugent.be.

[6]Throughout this paper the gas metallicity is expressed in solar units, using $\rm Z_\odot = 0.013$ as a reference value (Asplund et al. 2009).

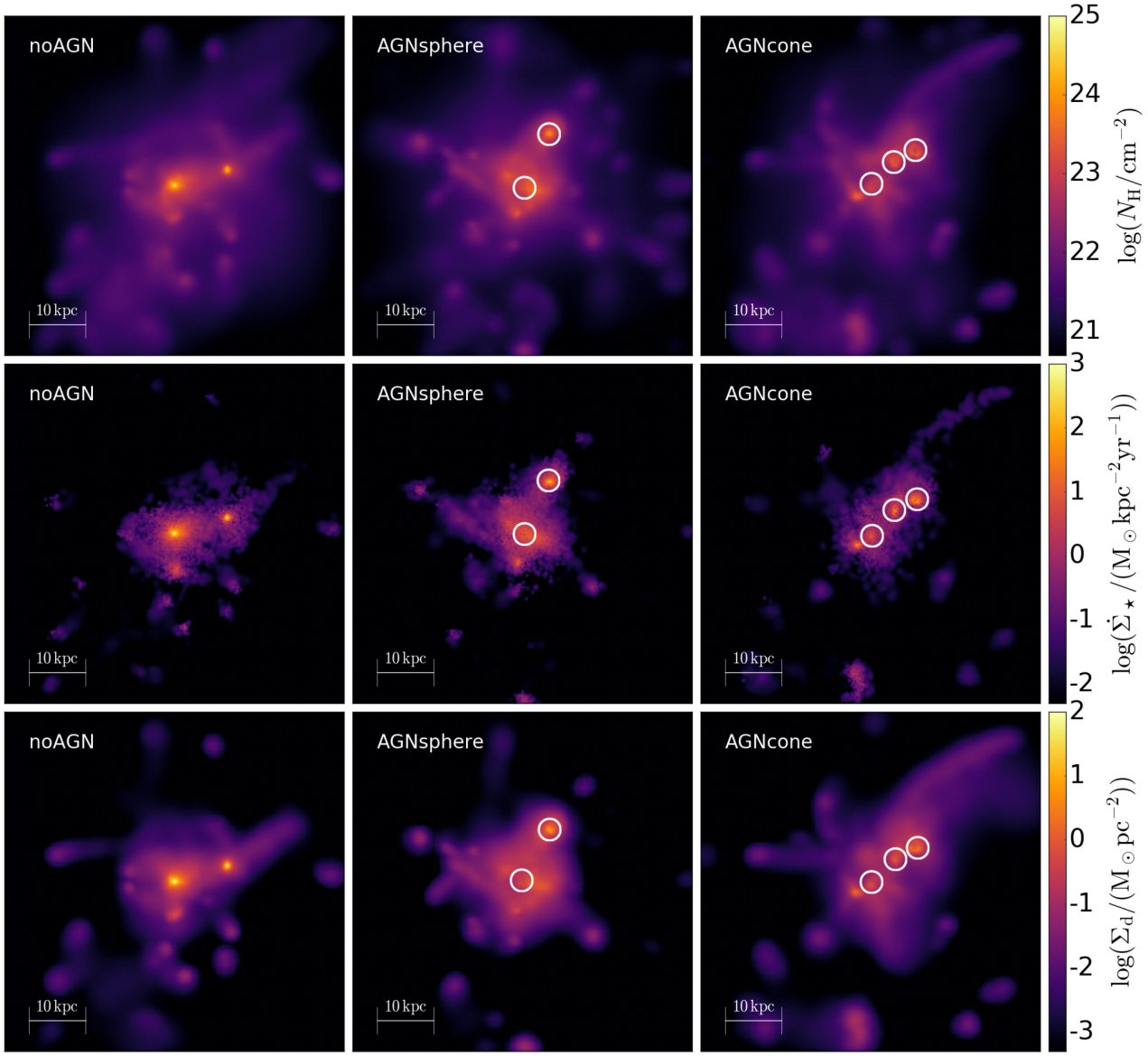

Figure 1. Morphology of the most massive halo at $z = 6.3$ inside a cubic box of 60 kpc size for the three cosmological simulations of B18: *noAGN* (left-hand column), *AGNsphere* (middle column) and *AGNcone* (right-hand column). The top, middle, and bottom panels show the hydrogen column density, the SFR and the dust surface density (assuming a dust-to-metal ratio $f_d = 0.08$, see Section 2.2.1), respectively. White empty circles show the location of BHs accreting at $\dot{M}_{BH} > 1\,M_\odot\,yr^{-1}$.

The dust surface density distribution derived in the $f_d = 0.08$ case is shown in the bottom row of Fig. 1. High dust surface density regions correspond to active star-forming regions where gas metal enrichment is more pronounced. Therefore, gas and dust density, and SFR are generally correlated in our simulations, as can be seen in Fig. 1.

The properties of dust as chemical composition and grain-size distribution are not known in early (AGN-host) galaxies. The nature and origin of dust at high redshift is in fact a widely debated topic (e.g. Valiante et al. 2009; Stratta, Gallerani & Maiolino 2011; Asano et al. 2013b; Hirashita et al. 2015; Hirashita & Aoyama 2019). Some works (Maiolino et al. 2004; Gallerani et al. 2010) have suggested that $z \gtrsim 4$ quasars require an extinction curve that is shallower than the Small Magellanic Cloud (SMC), possibly indicating the presence of SN-type dust (Todini & Ferrara 2001; Bianchi & Schneider 2007); however, the SMC extinction curve is instead favoured by the analysis of high-z quasars and GRBs performed by other research groups (Zafar et al. 2011; Hjorth et al. 2013; Zafar et al. 2018). For the time being, we assume a dust composition and grain-size distribution appropriate for the SMC by using the results[7] of Weingartner & Draine (2001). We defer the inclusion of an SN-type extinction curve to a future work.

2.2.2 *Dust implementation in* SKIRT

Dust is distributed in the computational domain in an octree grid with a maximum of eight levels of refinement for high dust-density regions, achieving a spatial resolution of ≈230 pc in the most refined cells, comparable with the softening length in the hydrodynamic

[7]We consider the revised optical properties evaluated in Draine (2003a, b, c).

simulation (≈200 physical pc at $z = 6.3$).[8] We verify in Appendix A that the number of refinement levels adopted in our fiducial setup is sufficient to achieve converge of the results. Adopting an SMC-like dust, the grain size distribution of graphite and silicates is sampled with 5 bins for each component. Gas particles hotter than 10^6 K, are considered dust-free as at these temperatures thermal sputtering is very effective at destroying dust (Draine & Salpeter 1979; Tielens et al. 1994; Hirashita et al. 2015). This assumption does not affect the main results of our work, as discussed in Appendix B.

Grain temperature and emissivity are evaluated by imposing energy balance between the local radiation field and dust re-emission. By default, when dust emission photons propagate, SKIRT accounts for the self-absorption by dust, but it does not take this absorption into account when computing the dust temperature, unless the self-absorption flag is turned on. As this effect may be relevant if dust is IR optically thick, we have enabled a self-consistent evaluation of the dust temperature, iterating the RT calculation for dust absorption and re-emission until the dust IR luminosity converges within 3 per cent.

We also include non-local thermal equilibrium corrections to dust emission, which include the contribution from small grains that are transiently heated by individual photons. In this case, grains of different sizes are no longer at a single equilibrium temperature, but follow a temperature distribution. Behrens et al. (2018) found in their calculations that stochastic heating affects mostly the MIR portion of the SED (rest-frame wavelength $\lesssim$80 μm) but it has a minor impact on the FIR and (sub)mm emission.

We do not include heating from CMB radiation. As discussed in Section 3.2, only a small fraction of dust grains is at a temperature comparable to $T_{\rm CMB}$. We expect this effect to be negligible, as seen a posteriori from the RT results.

We do not include any subgrid model for dust clumpiness. Recent works (e.g. Camps et al. 2016; Trayford et al. 2017; Liang et al. 2021) that account for subresolution structures of birth clouds harboring young stars (Jonsson, Groves & Cox 2010), whose typical scales are not resolved by the hydrodynamical simulations, are based on SED templates (Groves et al. 2008) not consistent with our fiducial set up. The stellar emission in the Groves et al. (2008) template is, in fact, calculated from Starbust99 models (Leitherer et al. 1999), by assuming a Kroupa (2002) IMF, whereas we model stellar emission using the Bruzual & Charlot (2003) model (see Section 2.2.3), based on the Chabrier (2003) IMF. Moreover, they include PAH molecules in the dust composition that are instead not considered in our work. We notice that Liang et al. (2021) find that the Groves et al. (2008) template mainly affects the IR emission from PAHs which is enhanced up to 50 per cent (see fig. 23 of their paper). Given that in our model we adopt an SMC dust composition (i.e. no PAHs), we do not expect that the inclusion of a subgrid model that accounts for dust clumpiness would significantly affect the main results of our work.

[8]When distributing the dust content derived from the hydrodynamical simulation into an octree grid, a kernel-based interpolation is required in order to convert the dust content from a particles-based distribution into an octree geometry. This procedure leads to a discrepancy between the total amount of dust carried by the SPH gas particles imported from the hydrodynamical simulation and the effective dust content in the computational domain used for the RT calculation. Therefore, it is important to check that the structure of the dust grid adopted achieves sufficient convergence relative to the overall dust content. We find that the relative difference in the overall dust content is within 0.1, 0.2, and 0.4 for *noAGN*, *AGNsphere* and *AGNcone*, respectively.

2.2.3 Radiation from stars and AGN

The UV radiation field mainly responsible for dust heating is provided by stellar sources and BHs. We describe in the following how the two components are implemented in our model.

Stellar particles in the simulation represent a single stellar population, i.e. a cluster of stars formed at the same time and with a single metallicity. Given the mass, age, and metallicity of the stellar particle imported, SKIRT builds the individual SEDs according to the Bruzual & Charlot (2003) family of stellar synthesis models, placing the sources at the locations of the stellar particles.

BHs are treated as point-source emitters as the typical sizes of the accretion disc and the dusty torus are much smaller ($\lesssim$10 pc) than the width of the most refined grid cells (≈230 pc, see Section 2.2.1). We implement their emission in SKIRT adopting a SED as described in Section 2.2.4.

The radiation field is sampled using a grid covering the *rest-frame* wavelength range[9] $[0.1 - 10^3]$ μm. The choice of the lower limit is quite common for RT simulations in dusty galaxies (Schneider et al. 2015; Behrens et al. 2018) and it is motivated by the fact that codes like SKIRT typically do not account for the hydrogen absorption of ionizing photons ($\lambda < 912$ Å). The choice of 10^3 μm as the upper limit of the wavelength grid is motivated by the fact that the intrinsic emission from stars and BHs is negligible above this limit. The base wavelength grid is composed of 200 logarithmically spaced bins.

A total of 10^6 photon packets per wavelength bin is launched from each source, i.e. stellar particles and BHs.[10] We collect the radiation escaping our computational domain for the six lines-of-sight perpendicular to the faces of the cubic computational domain.

2.2.4 AGN SED

The SED of an AGN is shaped by the numerous physical mechanisms involved in the process of gas accretion on to the BH (see Netzer 2015 for a comprehensive review on this topic). AGN SED templates are typically based both on theoretical arguments and observations (e.g. Shakura & Sunyaev 1973; Vanden Berk et al. 2001; Sazonov, Ostriker & Sunyaev 2004; Manti et al. 2016; Shen et al. 2020), possibly including the dusty torus modelling (Schartmann et al. 2005; Nenkova et al. 2008; Stalevski et al. 2012, 2016). For this work, we adopt a composite power-law for the AGN emission written as

$$L_\lambda = c_i \left(\frac{\lambda}{\mu\mathrm{m}}\right)^{\alpha_i} \left(\frac{L_{\rm bol}}{\mathrm{L}_\odot}\right) \mathrm{L}_\odot\ \mu\mathrm{m}^{-1}, \tag{4}$$

where i labels the bands in which we decompose the spectra and the coefficients c_i are determined by imposing the continuity of the function based on the slopes α_i. The coefficients c_i and α_i adopted and the relative bands are reported in Table 2 and they are chosen as described in the following.

For the X-ray band, based on the results by Piconcelli et al. (2005) and Fiore et al. (1994) in the hard (2–10 keV, $\alpha_{\rm X,hard} = -1.1 \pm 0.1$) and soft (0.5–2 keV, $-0.7 < \alpha_{\rm X,soft} < 0.3$) band, respectively, we

[9]The total AGN bolometric luminosity is distributed from the X-ray to the IR according to the SED adopted (see Section 2.2.4). The choice of the wavelength range adopted in our simulations affects the fraction of the AGN bolometric luminosity that effectively enters in the calculation (see Fig. 2). For the *fiducial* SED introduced in Section 2.2.4, this fraction is ≈60 per cent, whereas it is ≈40 per cent for the *UV-steep* SED.

[10]We verified that the number of packets used is sufficient to achieve numerical convergence by comparing the results with control simulations with 5×10^5 photon packets per wavelength bin.

Table 2. Coefficients of our AGN SEDs models as expressed in equation 4. The slopes α_i and the ranges of the piece-wise decomposition were chosen as explained in Section 2.2.4. Imposing the continuity of the function determines the coefficients c_i. The SED built in this way is by construction normalized to the bolometric luminosity of the source expressed in $L_\odot$ according to equation (4).

	Hard X (2–10) keV	Soft X [6.2 − 60] Å	X to EUV [50–600] Å	EUV [600–912] Å	UV to NIR [0.0912 − 5] μm	NIR to FIR [5 − 10^3] μm
c (fiducial)	2	0.042	14.133	1.972	0.111	6.225
α (fiducial)	− 1.1	− 0.7	0.4	− 0.3	− 1.5	− 4.0
c (UV-steep)	0.003	0.066	22.499	3.140	0.026	0.402
α (UV-steep)	− 1.1	− 0.7	0.4	− 0.3	− 2.3	− 4.0

consider $\alpha_{X,hard} = -1.1$ and $\alpha_{X,soft} = -0.7$. Consistently with Shen et al. (2020), in the wavelength range 50–600 Å, we use $\alpha = 0.4$ (the slope chosen for the soft X-ray band is then adopted up to 50 Å for continuity). For the Extreme UV band (EUV, $600 < \lambda < 912$ Å), we use $\alpha_{EUV} = -0.3$ as in Lusso et al. (2015). We also note that this value is consistent with the constraints by Wyithe & Bolton (2011, $-1.0 < \alpha_{EUV} < -0.3$) based on the analysis of near-zones observed around high-redshift quasars.

The analysis of a large sample (4576) of $z \lesssim 2.2$ quasars (Richards et al. 2003) spectra in the range $1200 \lesssim \lambda \lesssim 6000$ Å has shown that the spectral slopes are distributed in the range ($-2.6 < \alpha < -0.2$) and peak around $\alpha = -1.6$. In the $912 < \lambda < 2500$ Å band, Lusso et al. (2015) have constructed a stacked spectrum of 53 quasars at $z \sim 2.4$ finding $\alpha = -1.39 \pm 0.01$. Moreover, Gallerani et al. (2010) have analysed 33 quasars in the redshift range $3.9 \lesssim z \lesssim 6.4$ finding that unreddened quasars are characterized by $\alpha = -1.7 \pm 0.5$, whereas reddened quasars prefer steeper slopes ($\alpha < -2.3$). Finally, from a theoretical point of view, the classical black-body composition for a Shakura & Sunyaev (1973)-disc predicts that $F_\nu \propto \nu^{1/3}$, which translates into $\alpha = -2.3$. Given the uncertain value of the slope for wavelengths longer than 912 Å, we consider two possible values for the slope in the range from the UV to NIR: $\alpha_{UV} = -1.5$, which is representative of unreddened quasars, and $\alpha_{UV} = -2.3$. We will refer to these two models as the *fiducial* and *UV-steep* model, respectively.

At longer wavelengths, the intrinsic AGN emission is expected to follow the Rayleigh–Jeans tail regime $F_\nu \propto \nu^2$, which corresponds to $\alpha_{IR} = -4$. The transition between the UV slope and the IR one increases with the BH mass (Shakura & Sunyaev 1973; Pringle 1981; Sazonov et al. 2004). In this work, we adopt a transition wavelength $\lambda_{trans} = 5$ μm. This component represents the IR emission from the accretion disc only. We did not include the emission from the hot dust component from the torus because we cannot resolve the scales (1–10 pc) of the torus itself. We discuss how this affects our results in Section 5.1.

The fiducial and UV-steep SEDs adopted in this work are shown in Fig. 2 with blue and red lines, respectively. We also report with a green line the SED derived by Shen et al. (2020). Our bolometric corrections[11] (reported in Table 3) are consistent with the ones by Shen et al. (2020) (reported in the top panel of their fig. 2), for $L_{bol} \approx 10^{47}$ erg s^{-1}. We further calculate the $\alpha_{OX} = 0.384 \log L_\nu(2\text{keV})/L_\nu(2500\ \text{Å})$ index for our SEDs and find that it is in agreement with observations of $z \sim 6$ quasars (e.g. Nanni et al. 2017; Gallerani et al. 2017b; Vito et al. 2019a).

[11]Consistently with Shen et al. (2020), we express the UV band luminosity as $\nu_{1450\ \text{Å}} L_{\nu_{1450\ \text{Å}}}$, the B band as $\nu_{4400\ \text{Å}} L_{\nu_{4400\ \text{Å}}}$, whereas the soft [hard] X-ray luminosity is the integrated luminosity in the 0.5–2 [2–10] keV band.

3 RESULTS

We perform RT calculations on the three hydrodynamic simulations presented in Section 2.1. For each hydrosimulation, we vary the dust to metal ratio from $f_d = 0.08$ to 0.3; for the *AGNcone* run we consider both the AGN SEDs described in Section 2.2.4. We end up with a total of eight post-processed runs, as reported in Table 4.

In this section, we present the results obtained through our RT calculations. We first present in Section 3.1 the morphology of the UV (1000–3000 Å) and TIR (8–1000 μm) emission and discuss how it is affected by the presence of the AGN and total dust content. Then, in Section 3.2, we derive the dust temperature in the different runs. Finally, we discuss in Section 3.3 the synthetic SEDs resulting from our calculations.

3.1 Overview

In Fig. 3, we show the UV (top row) and TIR (middle row) emission maps derived for the runs *noAGN* (left-hand column), *AGNsphere* (middle column), *AGNcone* (right-hand column) for $f_d = 0.08$. In Fig. 4, we show the same maps but for $f_d = 0.3$. We use the same line of sight as in Fig. 1.

By comparing the TIR maps with the dust surface density (Fig. 1, bottom row), we see that the morphology of the TIR emission matches the dust distribution, as expected. Moreover, the brightest TIR spots in the *noAGN* (AGN runs) correspond to the locations of the most highly star-forming regions (accreting BHs), responsible for the dust grains heating. We discuss in more details the dust temperature in Section 3.2.

For what concerns UV emission, in the *noAGN* case, its distribution correlates with the star formation surface density (see middle row in Fig. 1); in the AGN runs, the brightest spots are located in correspondence of the AGN positions, identified by white circles. Noticeably, whereas in the *AGNcone* simulation with $f_d = 0.08$ three peaks appear in the UV emission map (labelled as A, B, and C in Fig. 3), corresponding to the AGN positions,[12] in the case $f_d = 0.3$ only one of them survives to the strong dust obscuration. In Section 4.1, we investigate in further details the contribution to the total SED of the different components traced by the UV and TIR maps.

Table 5 reports the UV and TIR luminosities before and after the dust-reprocessing of the radiation. We find that, in the *noAGN* run 84 − 94 per cent of the total UV emission is extincted by dust if $f_d = 0.08$–0.3. For comparison, in the *AGNcone* and *AGNsphere* runs, the same fraction is 77−99 and 54−95 per cent, respectively. Overall, we

[12]The accretion rate quoted in Table 2.1 for the case *AGNcone* is in fact the sum of the accretion rates of the most active BHs in the simulations ($\dot{M}_{BH} \approx$ 32, 7, and 50 M$_\odot$ yr^{-1}, for the sources A, B, and C, respectively).

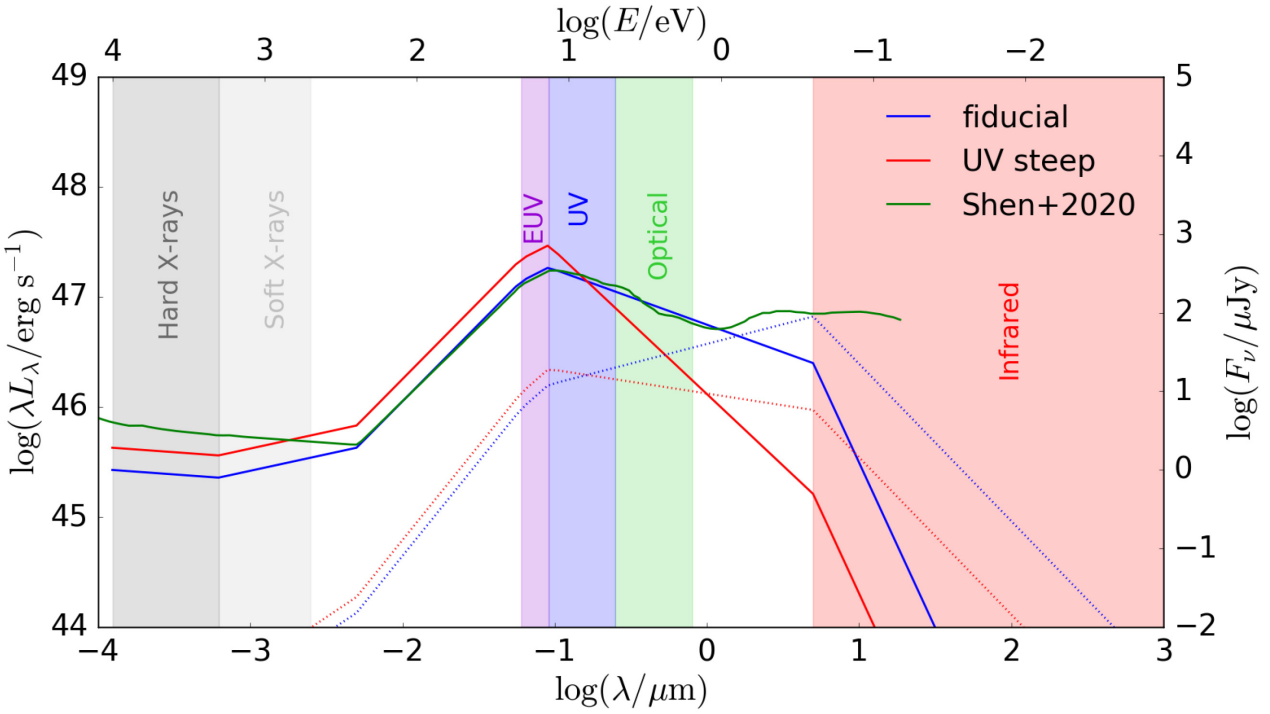

Figure 2. AGN SED for a bolometric luminosity $L_{\rm bol} = 10^{13} L_{\odot}$: the *fiducial* SED ($\alpha_{\rm UV} = -1.5$) is shown with a blue thick line; the *UV-steep* SED ($\alpha_{\rm UV} = -2.3$) is shown with a red thick line. We plot the SED template derived in Shen et al. (2020) for comparison with a thick green line, re-scaling it in order to have the same $L_{2500\,\text{Å}}$ of the fiducial SED. The SEDs differ mainly at wavelength longer than the UV band, with the UV-steep SED dropping faster than the other two. The fiducial SED is in very good agreement with the Shen et al. (2020) SED up to ≈2 μm, from where the contribution by dust in the torus and in the galaxy included in their IR template begins to dominate the emission in their SED. As a reference for the SED plots in the following, we also plot our two SEDs as the F_ν (in μJy) versus λ with dotted lines, keeping the same colour legend.

Table 3. Bolometric corrections ($L_{\rm bol}/L_{\rm band}$) and $\alpha_{\rm OX}$ for the *fiducial* ($\alpha_{\rm UV} = 1.5$) and *UV-steep* ($\alpha_{\rm UV} = 2.3$) AGN SED models adopted in this work. The bands used to compute the bolometric corrections are defined as: hard X-ray [2–10] keV, soft X-ray [0.5–2] keV, UV [0.1 − 0.3] μm. $L_{\rm B}$ is defined as λL_λ at $\lambda = 4400$ Å. The two models mostly differ for the luminosity in the *B* band. For a bolometric luminosity $L_{\rm bol} = 10^{47}$ erg s^{-1}, our bolometric corrections are consistent with the observational constraints reported in the top panel of fig. 2 by Shen et al. (2020).

SED model	$\frac{L_{\rm bol}}{L_{\rm X,hard}}$	$\frac{L_{\rm bol}}{L_{\rm X,soft}}$	$\frac{L_{\rm bol}}{L_{\rm UV}}$	$\frac{L_{\rm bol}}{L_{\rm B}}$	$\alpha_{\rm OX}$
Fiducial	130	130	3.4	6.0	−1.65
UV-steep	80	81	3.1	13.6	−1.51

find that in our simulated dusty galaxies ($M_{\rm d} \gtrsim 3 \times 10^7\,{\rm M}_{\odot}$) a large fraction (≳50 per cent) of UV emission is obscured by dust, with some lines of sight characterized by 1 per cent of UV transmission.

The range reported for the UV reprocessed luminosity in Table 5 refers to the variation occurring along different lines of sights: the minimum and maximum values differ by a factor that can be as high as ∼6 in the AGN runs. We expect UV luminosity variations along different lines of sight even larger than the ones we find, if UV radiation would intersect dense, compact, dusty, MCs, whose sizes (≲100 pc) and complex internal structure (∼1–10 pc, Padoan & Nordlund 2011; Padoan et al. 2014; Vallini et al. 2017) are not resolved by of our simulations.

According to the Unified Model (Urry & Padovani 1995), the classification between Type I (unobscured) and Type II (obscured) AGN is based on the presence of a dusty, donut-like shaped structure that is responsible for anisotropic obscuration in the circumnuclear region (<10 pc). Our results show that large UV luminosity variations with viewing angle, in addition to the ones due to the torus, arise from the inhomogeneous distribution of dusty gas surrounding the accreting BH, on ISM scales (≳200 pc; see also Gilli et al. 2014).

3.2 Dust temperature

One of the key physical quantities derived from RT calculations is the mass-weighted dust temperature ($\langle T_{\rm d}\rangle_{\rm M}$). In what follows, we first describe how we compute the luminosity-weighted dust temperature ($\langle T_{\rm d}\rangle_L$, see Behrens et al. 2018; Sommovigo et al. 2020) and compare this value with $\langle T_{\rm d}\rangle_M$; then we discuss how the dust temperature is affected by the total amount of dust, and different types of UV sources (stars versus AGN).

3.2.1 *Luminosity- versus mass-weighted* T_d

To compute $\langle T_{\rm d}\rangle_L$, we assume that each dust cell emits as a grey body[13] $L_{\rm TIR} \propto M_{\rm d} T_{\rm d}^{4+\beta_{\rm d}}$, where $\beta_{\rm d}$ is the dust emissivity index.[14] $\langle T_{\rm d}\rangle_L$, finally depends on the total amount of dust $M_{\rm d}$ in the

[13]This approximation holds only for dust cells that are optically thin to IR radiation, although we caveat that a small number of cells in the simulation is actually optically thick.

[14]The actual value of $\beta_{\rm d}$ depends on the RT calculation. For example, Behrens et al. (2018) found a value of $\beta_{\rm d} = 1.7$. For computing the luminosity-weighted temperature, we assume $\beta_{\rm d} = 2$. This choice does not significantly affect the final results: the estimate of $\langle T_{\rm d}\rangle_L$ varying $1.5 < \beta_{\rm d} < 2.5$ is within 10 per cent of the value reported in Table 5.

Table 4. SKIRT post-processing runs performed. The first column labels the RT simulation, the second column indicates the corresponding hydrodynamical run, the third column specifies the radiation field included (e.g. stars with or without BHs), the fourth column specifies the AGN SED used (if BHs are present), and the fifth column contains the dust to metal ratio $f_{\rm d}$ adopted.

RT run name	Hydro run name	Radiation field	AGN SED	$f_{\rm d}$
noAGN008	noAGN	Stars		0.08
noAGN03	noAGN	Stars		0.3
AGNsphere008	AGNsphere	Stars + BHs	Fiducial	0.08
AGNsphere03	AGNsphere	Stars + BHs	Fiducial	0.3
AGNcone008	AGNcone	Stars + BHs	Fiducial	0.08
AGNcone03	AGNcone	Stars + BHs	Fiducial	0.3
AGNcone008UVsteep	AGNcone	Stars + BHs	UV-steep	0.08
AGNcone03UVsteep	AGNcone	Stars + BHs	UV-steep	0.3

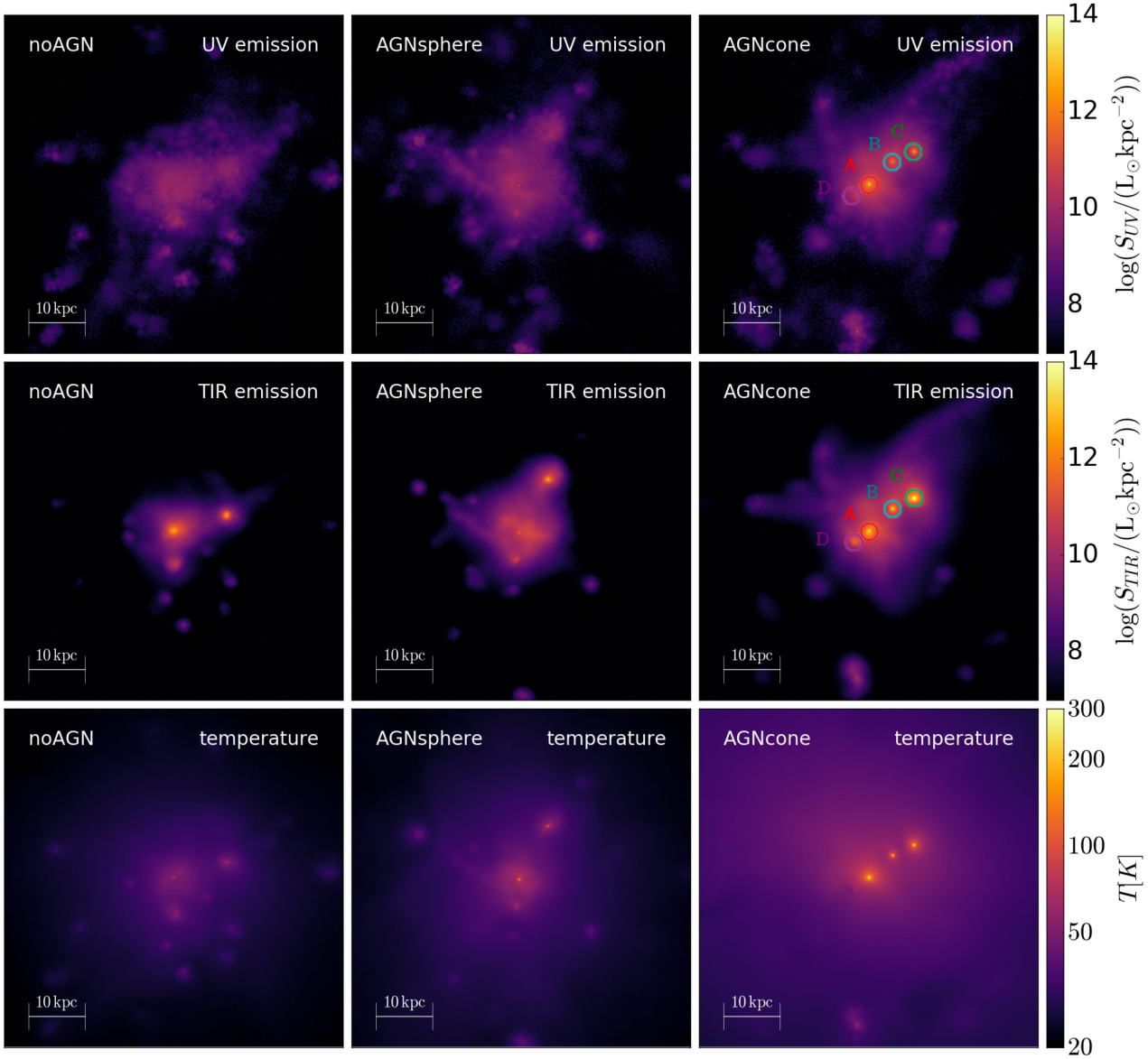

Figure 3. UV (top row), TIR (middle row), luminosity-weighted dust grain temperature (bottom row) maps for the runs with $f_{\rm d} = 0.08$. The maps shown are produced with the same line of sight used in Fig. 1. We mark the four most luminous sources in TIR for the *AGNcone* runs, which will be discussed in more details in Section 4.1.

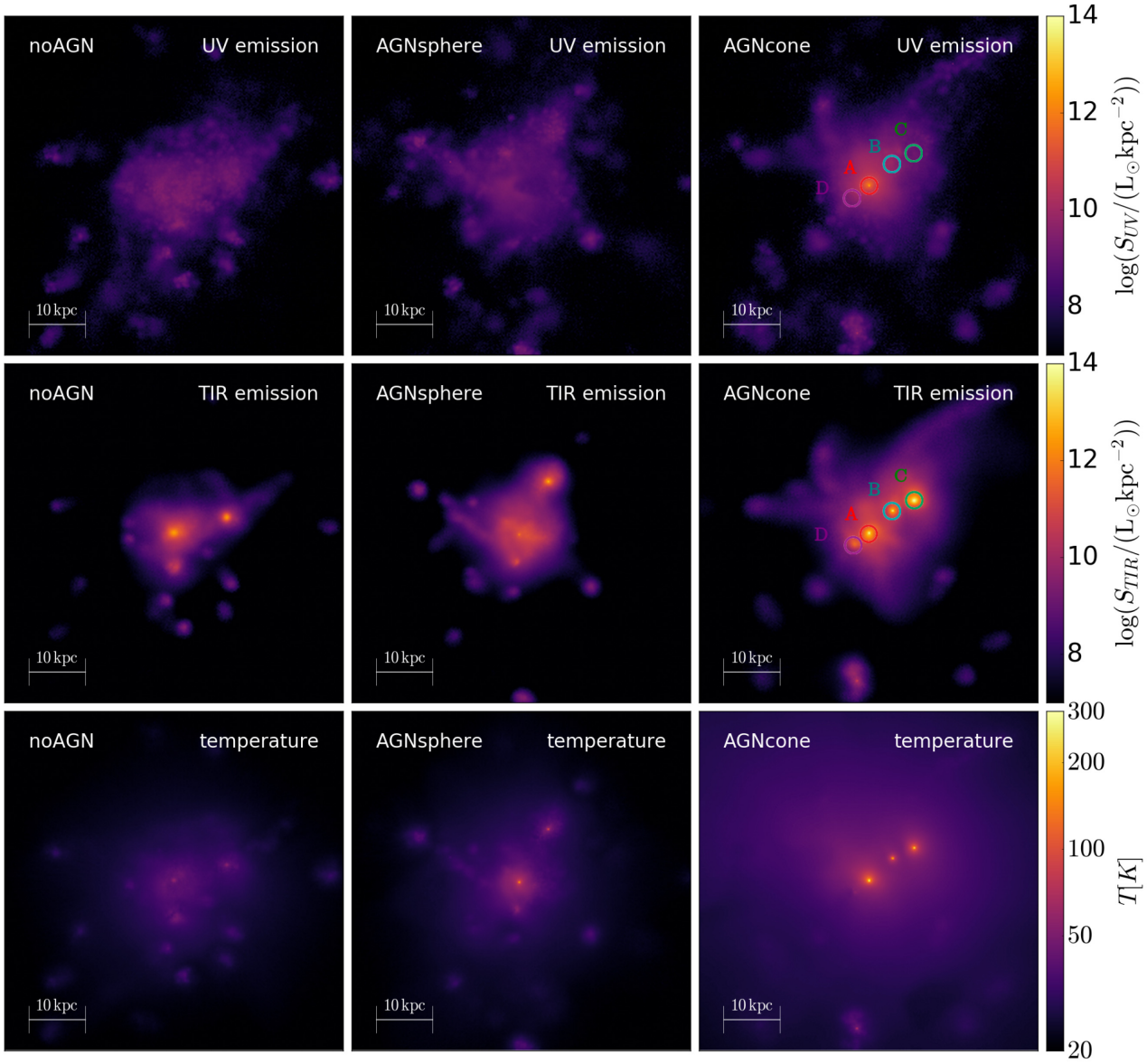

Figure 4. Same as in Fig. 3 but for for $f_\mathrm{d} = 0.3$.

Table 5. Overview of the main physical properties of the galaxies for the RT runs performed (see Table 1). The table contains: (first column) the name of the run, (second column) the processed UV (integrated in the band 1000–3000 Å) luminosity L_UV, (third column) the processed total IR (integrated in the band 8−1000 μm) luminosity L_TIR, (fourth column) the total dust mass contained in the simulated region M_d, (fifth column) the *luminosity-weighted* temperature of the dust grains $\langle T_\mathrm{d}\rangle_L$, reported as the mean of the PDF within one standard deviation, (sixth column) the minimum and maximum value the dust grains temperature, (seventh column) the intrinsic (i.e, not dust-processed) UV luminosity $L_\mathrm{UV}^\mathrm{intr}$, (eighth column) the effective UV optical depth τ_UV, estimated as $\mathrm{e}^{-\tau_\mathrm{UV}} = L_\mathrm{UV}/L_\mathrm{UV}^\mathrm{intr}$. For the dust-processed UV, TIR luminosities, and UV optical depth we report the range bracketed by the six line of sights considered for each simulation.

RT run	L_UV $(10^{11} L_\odot)$	L_TIR $(10^{12} L_\odot)$	$\mathrm{M_d}$ $(10^7\ \mathrm{M}_\odot)$	$\langle T_\mathrm{d}\rangle_L$ (K)	$T_\mathrm{d}^\mathrm{min/max}$ (K)	L_UV^{intr} $(10^{12}\ L_\odot)$	τ_UV
noAGN008	5.7–6.7	4.4–4.6	9.2	54 ± 6	15–64	4.1	1.81–1.97
noAGN03	3.2–3.9	4.7–4.9	34	48 ± 6	13–57	4.1	2.35–2.56
AGNsphere008	7.0–17	3.3–3.4	5.1	70 ± 27	17–179	3.7	0.78–1.65
AGNsphere03	2.8–7.9	4.4–4.6	19	62 ± 25	15–178	3.7	1.54–2.57
AGNcone008	27–90	43–50	3.3	208 ± 78	22–282	39	1.47–2.67
AGNcone03	5.8–32	54–71	13	182 ± 69	20–272	39	2.50–4.20

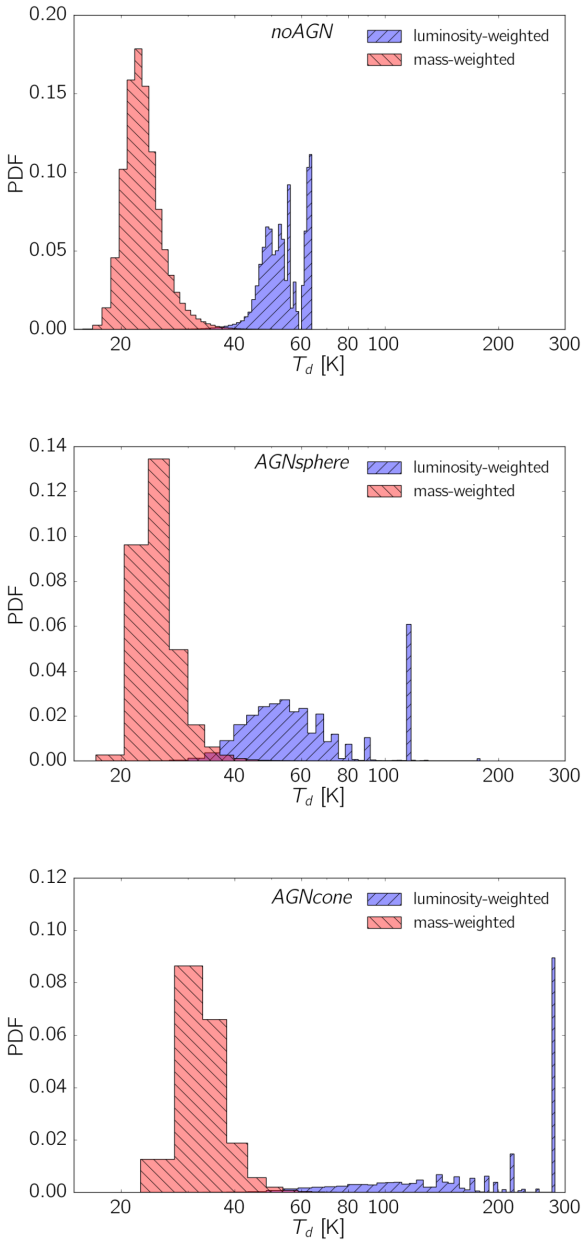

Figure 5. Mass-weighted (red histograms) and luminosity-weighted (blue histograms) dust grains temperature PDF. The panels refer to *noAGN* (top panel), *AGNsphere* (middle panel) and *AGNcone* (bottom panel) . As a reference case, we show the results for $f_{\rm d} = 0.08$.

simulation, determined by our choice of $f_{\rm d}$. Runs with $f_{\rm d} = 0.3$ are characterized by average dust temperatures ∼10 per cent lower with respect to the corresponding runs with $f_{\rm d} = 0.08$. This is because the same UV energy is distributed over a larger amount of dust mass.

In Fig. 5, we show the $\langle T_{\rm d}\rangle_L$ PDF (blue histograms), compared with the mass-weighted $\langle T_{\rm d}\rangle_M$ one (red histograms) for the *noAGN*, *AGNsphere*, and *AGNcone* simulations with $f_{\rm d} = 0.08$, as a reference case. In each run, the PDF of $\langle T_{\rm d}\rangle_M$ peaks at lower dust temperatures with respect to $\langle T_{\rm d}\rangle_L$. The difference between the mass-weighted and luminosity-weighted temperatures is particularly evident in the runs in which AGN radiation is included. In particular, the spikes of the luminosity-weighted histograms correspond to dust cells in the immediate proximity of accreting BHs. This dust component constitutes only a small fraction of the total mass, but it provides a significant contribution to the overall luminosity, as further discussed in the next section.

3.2.2 *Stars and AGN contribution to dust heating*

The brightest TIR spots in Figs 3 and 4 in the *noAGN* (AGN runs) correspond to the locations of the most highly star-forming regions (accreting BHs). Whereas in the *noAGN* run the maximum $T_{\rm d}$ value is about 60 K, in the AGN runs, dust grains reach luminosity-weighted temperatures $T_{\rm d} \gtrsim 200$ K close to BHs, and $T_{\rm d} \approx 60$ K in the diffuse gas.

We underline that in the *noAGN* run $\langle T_{\rm d}\rangle_L$ is up to four times lower with respect to the AGN runs despite having an SFR three times higher. These results indicate the dominant role played by AGN radiation in the dust heating. This is particularly evident if we compare in more details the run *noAGN* and *AGNsphere*. In the *noAGN* case, $L_{\rm UV}^{\rm intr} = L_{\rm UV,stars} = 4.1 \times 10^{12}\, L_{\odot}$; in the *AGNsphere* case, $L_{\rm UV}^{\rm intr} = L_{\rm UV,stars} + L_{\rm UV,BH} = (2.3 + 1.4) \times 10^{12} L_{\odot} = 3.7 \times 10^{12}\, L_{\odot}$.

Thus, although the UV budget in the *AGNsphere* run is mostly provided by stars, and the total UV intrinsic luminosity is comparable to the *noAGN* case, $T_{\rm d}$ peaks at higher temperature values if BH accretion is present. In Fig. 6, we compare the fraction of mass (left panel) and TIR luminosity[15] (right-hand panel) from dust with a temperature above a certain threshold for the three runs. In the *noAGN* run, the TIR luminosity is arising from dust with $T_{\rm d} \lesssim 50$ K. In the *AGNsphere* (*AGNcone*) run >50 per cent of the TIR luminosity is arising from dust with $T_{\rm d} \gtrsim 70$ K ($T_{\rm d} \gtrsim 150$ K); this warm dust only constitutes 0.1 per cent of the total dust mass. This confirms that a small mass fraction of warm dust dominates the IR emission, as expected from the scaling $L_{\rm d} \propto M_{\rm d} T_{\rm d}^{4+\beta_{\rm d}}$.

3.2.3 *Spatial extent of FIR emitting regions*

Fig. 7 shows the fraction of dust mass and IR luminosity as a function of the distance[16] from the regions with the highest star formation for the *noAGN* case and from the BHs with the highest accretion rate for the run *AGNsphere* and *AGNcone*.

In the *noAGN* case, the dust mass within $r \lesssim 300$ pc represents ∼0.3 per cent of the total dust, and it provides ∼3 per cent of the total IR luminosity. In the *AGNsphere* (*AGNcone*) case, only ∼0.1 per cent (∼0.06 per cent) of the total dust mass is found at $r \lesssim 300$ pc from an accreting BH but it contributes 20 per cent (∼40 per cent) of the total IR luminosity.

3.3 Synthetic SEDs

Fig. 8 shows the intrinsic flux density from stars (dashed line) and AGN (dotted line) for the first six runs reported in Table 4. The higher value of the flux density from stars in the *noAGN* run with respect to both AGN runs is due to the negative AGN feedback that in the AGN

[15]The luminosity is computed assuming $\beta_{\rm d} = 2$ for consistency with the temperature PDF. The resulting luminosity varying $1.5 < \beta_{\rm d} < 2.5$ differs by ≈ 10 per cent from the quoted values.

[16]Given that there are multiple accreting BHs, we selected the two (3) most active ones in the *AGNsphere AGNcone* run and two most accreting star-forming regions (the main galaxy and its largest satellite) in the *noAGN* run. For each cell containing dust in the octree grid, we evaluate the distance from each reference source and then we consider the minimum one for this calculation.

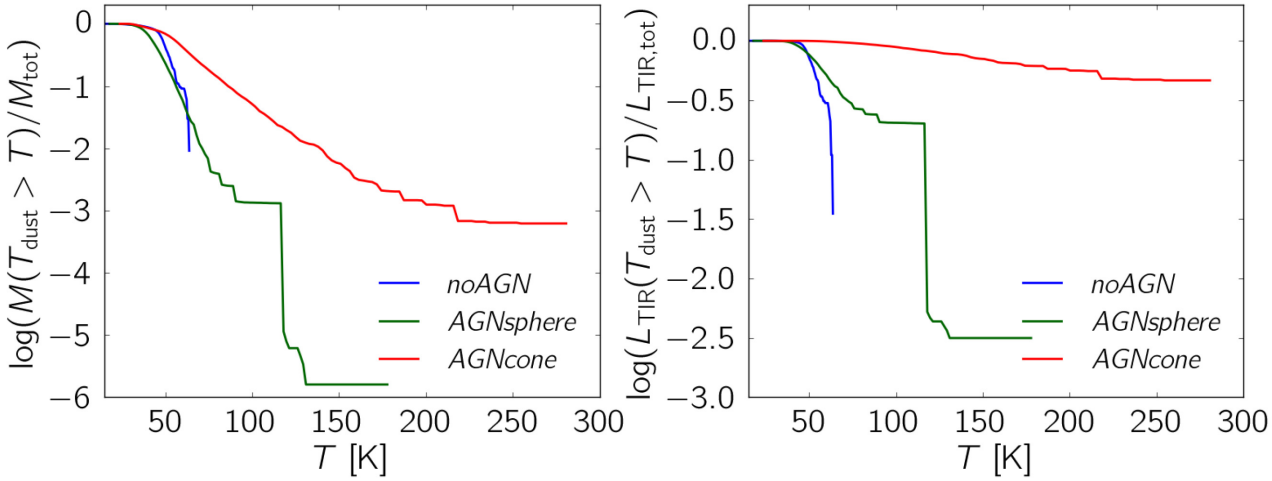

Figure 6. Mass fraction (left-hand panel) and TIR luminosity fraction (right-hand panel) of dust with a temperature $T_d > T$ as a function of the temperature T for the runs *noAGN* (blue line), *AGNsphere* (green line), *AGNcone* (red line). Results for $f_d = 0.08$ are shown.

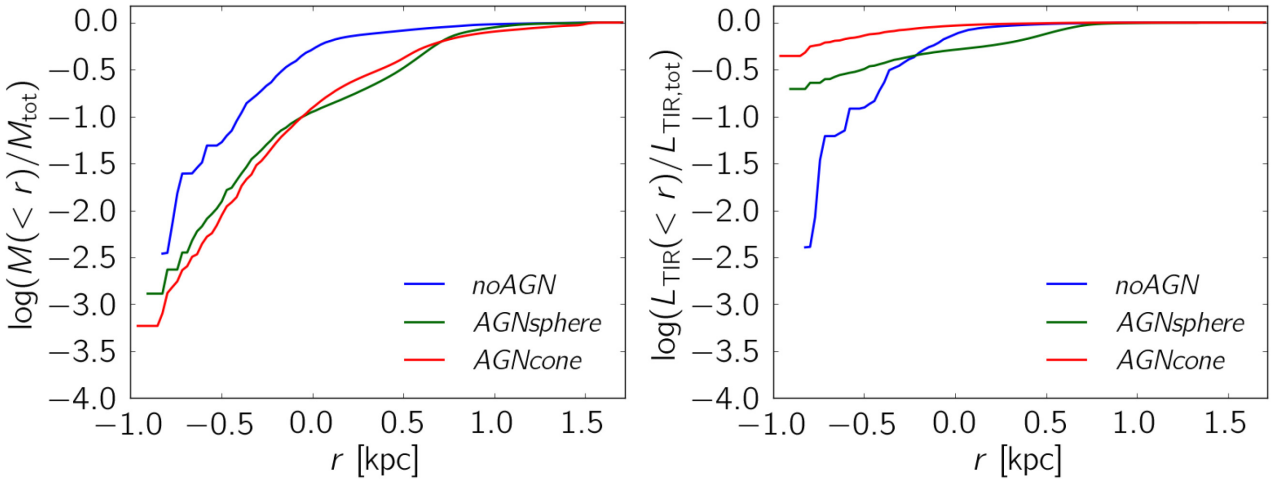

Figure 7. Cumulative mass fraction (left-hand panel) and TIR luminosity fraction (right-hand panel) of the dust at a distance r from AGN location or most star-forming regions. The lines show the results for *noAGN* (blue line), *AGNsphere* (green line) and *AGNcone* (red line) with $f_d = 0.08$.

simulations quenches the SFR in the host galaxy (see section 3.7 of B18 for an extensive discussion on this topic). This effect is more pronounced in the *AGNcone* run since it is characterized by a BH accretion rate that is a factor of ∼30 higher than in *AGNsphere* (see Table 1). The total intrinsic flux (dotted-dashed line) is comparable between *noAGN* and *AGNsphere* (see also Table 5).

We now analyse the differences between the reprocessed flux density (observed, solid line) resulting from our calculations, focusing on the rest-frame NIR ($1 \lesssim \lambda_{RF} \lesssim 5\,\mu m$), MIR ($5 \lesssim \lambda_{RF} \lesssim 40\,\mu m$), and FIR ($40 \lesssim \lambda_{RF} \lesssim 350\,\mu m$) wavelength ranges.

The intrinsic NIR flux is suppressed by ≈10 times in all runs; the highest rest-frame UV attenuation is seen in the *AGNcone* run, with some (all) lines of sight showing a flux reduced by ≈100 times for $f_d = 0.08$ ($f_d = 0.3$). However, for a fixed dust content, the *AGNcone* run still provides the highest rest-frame UV flux. In this wavelength range, the SED is nearly constant in the *noAGN* run whereas it increases toward larger wavelengths in the runs with AGN, as a consequence of the contribution from accretion. The observed optical-NIR flux depends both on the radiation field and dust content.

For what concerns the MIR, at short wavelengths, ($\lambda_{RF} \sim 4{-}6\,\mu m$), the SED is dominated by the almost unattenuated emission from stars and/or AGN; the *AGNcone* SED is ∼30 times brighter than the *AGNsphere* one as a consequence of its higher BH activity. At longer wavelengths ($\lambda_{RF} > 6\,\mu m$), the observed flux arises from heated dust IR emission. The flux density in this wavelength range is the result of the sum of multiple greybodies, each emitting at different temperatures, according to the luminosity-weighted dust temperature PDF discussed in Section 3.2.1. The warm dust in AGN runs produces a MIR excess with respect to the *noAGN* run, and shifts the peak of the emission toward shorter wavelengths: $\lambda^{peak}_{noAGN} = 59.4\,\mu m$, $\lambda^{peak}_{AGNsphere} = 54.1\,\mu m$ and $\lambda^{peak}_{AGNcone} = 27.0\,\mu m$.

Finally, the Rayleigh–Jeans tail of the FIR emission is mostly sensitive to the total dust content. In fact, by comparing the $f_d = 0.08$ and 0.3 cases, we find that the flux at 1 mm scales almost linearly with the dust mass, without a strong dependence on the radiation source.

To summarize, the SED in the NIR wavelength range depends both on the dust mass (for fixed dust properties) and the type of source

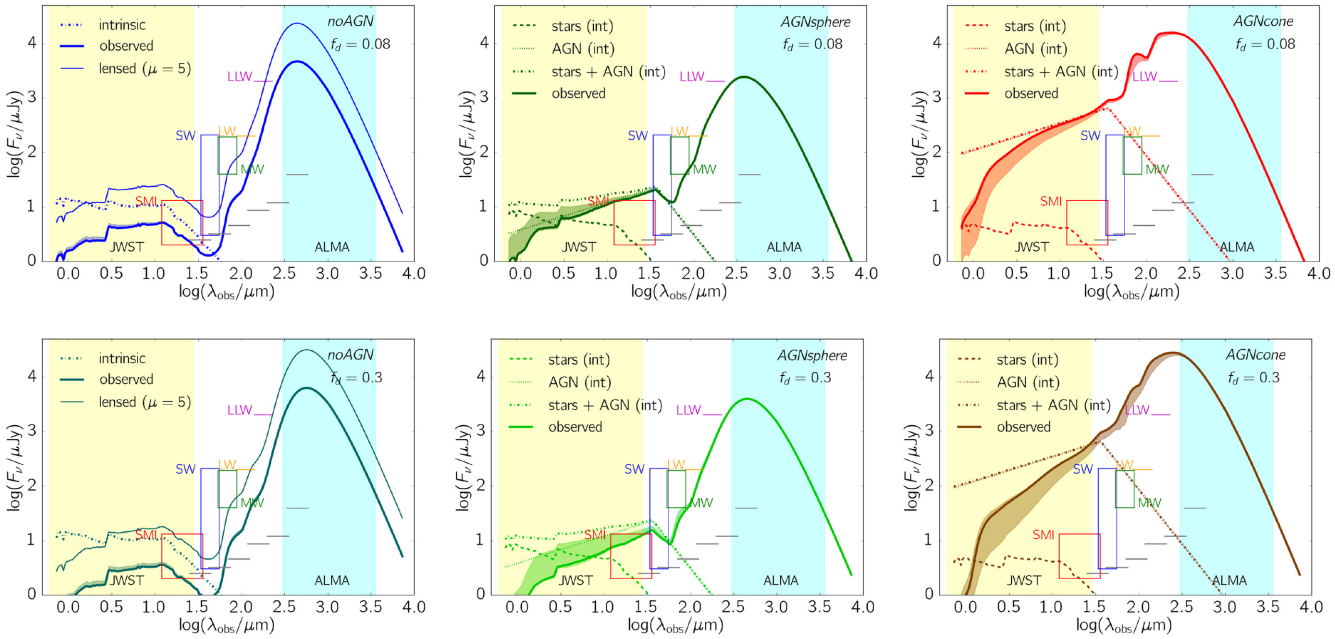

Figure 8. Intrinsic and processed (observed) SED for the first six runs in Table 4. The first column refers to *noAGN*, the second to *AGNsphere* and the third to *AGNcone*, whereas the first row to $f_d = 0.08$, and the second to $f_d = 0.3$. The solid line shows the observed flux for the reference line of sight, whereas the shaded area brackets the scatter in the observed SED between the six lines of sights used for the computation. The intrinsic flux is also shown with a dot-dashed line. In the runs with AGN, the individual components are also shown: radiation from stars is denoted with dashed lines, radiation from AGN with dotted lines. In *noAGN* runs, thin solid lines indicate the flux that would be observed if the galaxy is magnified by a factor $\mu = 5$. Sensitivity bands of *JWST* and ALMA are shown as yellow and cyan shaded regions respectively. The grey lines indicate the sensitivity reached by the ORIGINS telescope at 5σ in 1 h of observing time. The coloured rectangles and horizontal lines indicate the sensitivity of the two instruments of the SPICA telescope: SMI ($\lambda_{obs} = 27$ μm, red rectangle), and SAFARI, in photometric mapping mode at short (SW, $\lambda_{obs} = 45$ μm, blue rectangle), mid-panel (MW, $\lambda_{obs} = 72$ μm, green rectangle), long (LW, $\lambda_{obs} = 115$ μm, orange line) and very long wavelengths (LLW, $\lambda_{obs} = 185$ μm, violet line). The upper sides of rectangles represent the sensitivity that will be reached by SPICA at 5σ in 1 h of observing time. The bottom side of rectangles represents the maximum sensitivity reachable with SPICA, and it is obtained by considering the confusion limit flux at 3σ (such a high sensitivity can be reached in the case of follow-up observations). If the confusion limit is reached in less than 1 h, it is shown as a single line.

(stars and/or AGN); the MIR retains information almost solely on the type of source: the presence of an AGN enhances the flux and shifts the peak of the emission at shorter wavelengths; the flux in the Rayleigh–Jeans tail of the FIR emission mostly depends on the total dust content.

4 COMPARISON WITH $z \sim 6$ QUASAR DATA

To test the results of our model (SPH simulation post-processed with RT calculations), we compare in Fig. 9 our predictions from the *AGNcone* run ($M_{UV} = -27.97$) with multiwavelength (NIR to FIR) observations of $z \sim 6$ bright ($-29 \lesssim M_{UV} \lesssim -26$) quasars (see Table 6).

In the NIR, our predicted SEDs are underluminous with respect to the flux of TNG/GEMINI spectra (grey lines in Fig. 9). This mismatch cannot be solved by decreasing the dust content, since by assuming $f_d < 0.08$ the synthetic SEDs would become underluminous in the FIR with respect to ALMA data. We instead suggest that a better agreement with observations can be obtained by assuming an extinction curve flatter than the SMC (Gallerani et al. 2010, Di Mascia et al., in preparation).

For what concerns the comparison in the MIR, models with α_{UV}^{fid} are in good agreement both with *Spitzer/Herschel* photometric data and with the slope/shape of templates by Hernán-Caballero & Hatzimi-naoglou (2011) resembling *Spitzer*/IRS spectra. Vice versa, models with α_{UV}^{steep} are both underluminous with respect to *Spitzer*/IRAC observations at $\lambda_{obs} = 24$ μm (namely $\lambda_{RF} \sim 3$ μm at $z \sim 6$) and show a slope in the MIR that does not agree with observed spectra.

We underline that the model with α_{UV}^{steep} can be possibly reconciled with observations if the torus is included. In fact, a dust component with the temperature close to sublimation (∼1500 K) would enhance the MIR emission exactly at the *Spitzer*/IRAC wavelengths.[17] We give a first estimate of the impact of the torus emission on our predicted SEDs in Section 5.1 (Fig. 11) and we defer the inclusion of the torus into our model to a future study.

By comparing our predicted SEDs with FIR observations, we note that both models ($f_d = 0.08$–0.3) provide a reasonable match with FIR data, independently on the assumed UV slope (fiducial versus UV-steep). We find that the models with a larger dust-to-metal ratio $f_d = 0.3$ are slightly preferred, since in the $f_d = 0.08$ case we can only explain the less luminous FIR sources.

Hereafter, we consider as fiducial the model with α_{UV}^{fid} and $f_d = 0.3$.

4.1 Multiple merging system

The most massive halo in the *AGNcone* run at $z = 6.3$ hosts a merging system of multiple sources, three of which are AGN (A, B, C) and one is a normal star-forming galaxy (D). We show in Fig. 10 the SEDs extracted from individual sources. In our simulated system,

[17]The emission of a greybody at temperature T_d and with $\beta_d = 2$ peaks at $\lambda_{peak} = (2.9 \times 10^3)/T_d$ μm.

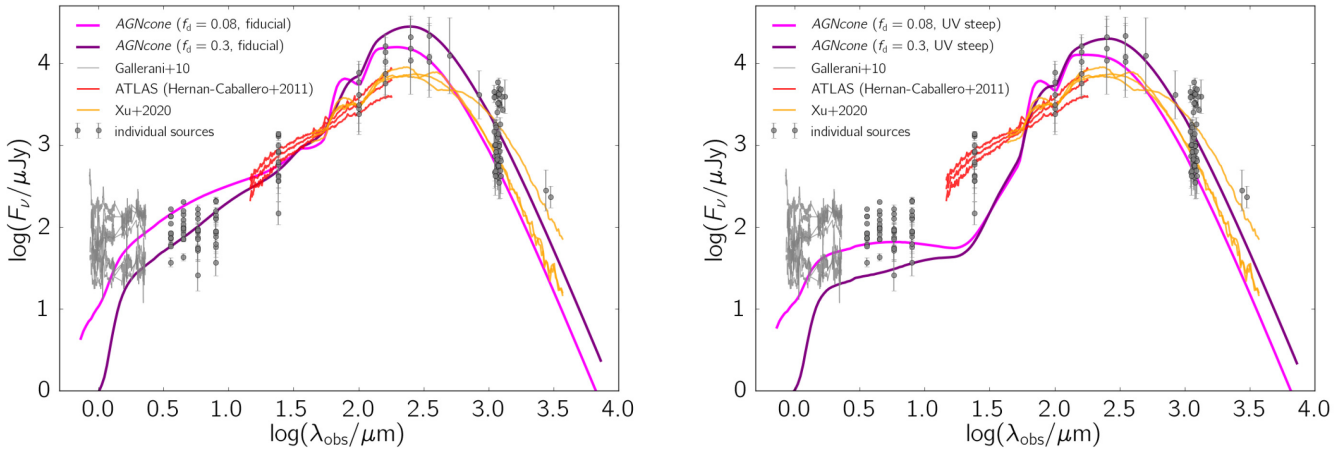

Figure 9. Left-hand panel: Comparison between synthetic fiducial SEDs and observations of $z \sim 6$ quasars (grey circles, see Table 6). The magenta and violet solid curves denote the models for $f_d = 0.08$ and 0.3, respectively. Grey lines represent dust-reddened $z \gtrsim 6$ quasar spectra taken with the TNG/GEMINI ($A_{3000} > 0.8$, see Table 1 in Gallerani et al. 2010). The spectra are calibrated by using the measures of λL_λ at 1450 Å provided in Table 1 by Juarez et al. (2009). We further show with orange lines the template obtained from the analysis of 125 quasar spectra at $0.020 < z < 3.355$ taken with *Spitzer*/IRS [the tree lines correspond to the median SED, the 25 and 75th percentiles, in the case of the luminous, $\log(\lambda L_{5100}) > 44.55$, sub-sample by Hernán-Caballero & Hatziminaoglou (2011)], and with red lines the IR AGN SED derived by Xu, Sun & Xue (2020) from 42 quasars at $z < 0.5$ (see their table 3). The spectra of these low redshift sources are reported to get a hint of the spectral slope of AGN in the MIR; no spectroscopy information is available so far in the case of $z \sim 6$ quasars. Right-hand panel: same as left-hand panel, but for the UV-steep AGN SED models.

source A is the most luminous UV source, providing ∼70 per cent of the total UV flux. However, it does not correspond to the most accreting BH, which is instead powering source C, distant ∼10 kpc from A. Despite having the highest intrinsic UV budget, this source is fainter than A in the UV because it is enshrouded by dust: Source C is in fact the most luminous IR source of the system and provides ∼70−80 per cent (∼40 per cent) of the MIR (FIR) flux. The second brightest UV source in our system is source D.

By comparing our synthetic SEDs with *HST* and ALMA data[18] (Decarli et al. 2017; Marshall et al. 2020), we found that sources A, B and D would be detectable and resolved with *HST*; for what concerns the FIR, given the angular resolution of current ALMA data (i.e. 1 arcsec that corresponds to ∼6 kpc at $z = 6.3$), it is not possible to disentangle source B and D from A, whereas source C would show up as an SMG companion, even brighter than source A (as in the case of CFHQ J2100-1715 by Decarli et al. 2017). To summarize, our study shows that, consistently with *HST* and ALMA observations, bright ($M_{UV} \leq -26$) $z \sim 6$ quasars (e.g. source A in our simulations) are part of complex, dust-rich merging systems, possibly containing highly accreting BHs (e.g. source A, B, and C with $\gtrsim 5\,M_\odot\,yr^{-1}$) and star-forming galaxies (e.g. source D). Deeper and higher resolution ALMA data and *JWST* observations are required to better characterize the properties of galaxy companions in the field of view of $z \sim 6$ quasars.

5 GUIDING FUTURE MIR FACILITIES

Given the good agreement between our results and currently available $z \sim 6$ quasars observations, we can use our simulations to make predictions for the proposed OST[19] (Wiedner et al. 2020). OST covers the wavelength range 2.8−588 μm, and is designed to make broad-band imaging (FIR Imager Polarimeter, FIP), low resolution ($R \sim 300$) wide-area/deep spectroscopic surveys, and high resolution ($R \sim 40\,000$–$300\,000$) pointed observations (with the Origins Survey Spectrometer). We further consider the capability of detecting IR emission from $z \sim 6$ quasars through a 2.5 m diameter IR telescope, cryocooled to 8 K that covers the wavelength range 12−230 μm, and is designed to make high-resolution ($R \sim 28\,000$) in the near-IR (12−18 μm) and MIR (30–37 μm) broad-band mapping, and small field spectroscopic and polarimetric imaging at 100, 200, and 350 μm. These are the characteristics of the Space Infrared Telescope for Cosmology and Astrophysics (SPICA; e.g. Spinoglio et al. 2017; Gruppioni et al. 2017; Egami et al. 2018; Roelfsema et al. 2018), an IR space mission, initially considered as a candidate for the M5 mission, but cancelled in 2020 October (Clements, Serjeant & Jin 2020).

The *noAGN* case is detectable by ORIGINS in five bands, corresponding to ≈ 6−80 μm rest-frame. ORIGINS would be able to probe the SED of highly star-forming galaxies (SFR ∼ 600 $M_\odot\,yr^{-1}$) at wavelengths shorter than the peak wavelength, which is crucial in order to have a solid determination of the dust temperature (Behrens et al. 2018; Sommovigo et al. 2020). The *noAGN* case falls just below the SPICA sensitivity threshold. We thus consider the possibility of observing lensed galaxies with SPICA; the thin solid SED in the *noAGN* panels in Fig. 8 accounts for a magnification factor $\mu \sim 5$. Our results show that highly star-forming galaxies (SFR ∼ 600 $M_\odot\,yr^{-1}$) without an active AGN will be at the SPICA reach if lensed by a factor $\mu \gtrsim 5$.

For what concerns the *AGNsphere* case, the simulated run corresponds to a faint AGN ($M_{UV} = -23.4$; X-ray luminosity $L_X \sim 10^{44}$ erg s^{-1}). This kind of sources is not easily detectable through

[18]We do not consider constraints from MIR observations since individual sources cannot be resolved at these wavelengths as a consequence of the poor angular resolution. We further refer to Vito et al. in preparation for a detailed comparison with X-ray observations.

[19]OST is a concept study for a 5.9 m diameter IR telescope, cryocooled to 4.5 K, that has been presented to the United States Decadal Survey in 2019 for a possible selection to NASA's large strategic science missions.

Table 6. Quasars used for the comparison with the prediction by our model. Columns indicate: source name (first), redshift (second), $M_{\rm UV}$ (third) and references for the photometric data used in the comparison (fourth), according to the legend. [1] Gallerani et al. (2010); [2] Juarez et al. (2009); [3] Walter et al. (2003); [4] Bertoldi et al. (2003b); [5] Riechers et al. (2009); [6] Gallerani et al. (2014); [7] Stefan et al. (2015); [8] Leipski et al. (2014); [9] Venemans et al. (2018); [10] (Wang et al. 2016); [11] (Venemans et al. 2012); [12] (Venemans et al. 2017b); [13] (Willott, Bergeron & Omont 2017); [14] (Mazzucchelli et al. 2017); [15] (Venemans et al. 2016).

Source	z	$M_{\rm UV}$	Reference
J1030+0524	6.31	−27.12	[1-2,8]
J1048+4637	6.23	−27.60	[1-2,8]
J1148+5251	6.43	−27.85	[1-8]
J1306+0356	6.03	−26.76	[1-2,8-9]
J1602+4228	6.07	−26.85	[1-2,8]
J1623+3112	6.25	−26.71	[1-2,8]
J1630+4012	6.07	−26.16	[1-2,8]
J0353+0104	6.07	−26.56	[8]
J0818+1722	6.00	−27.44	[8]
J0842+1218	6.08	−26.85	[8,9]
J1137+3549	6.01	−27.15	[8]
J1250+3130	6.13	−27.18	[8]
J1427+3312	6.12	−26.48	[8]
J2054-0005	6.04	−26.15	[8]
P007+04	6.00	−26.58	[9]
P009-10	6.00	−26.50	[9]
J0142-3327	6.34	−27.76	[9]
P065-26	6.19	−27.21	[9]
P065-19	6.12	−26.57	[9]
J0454-4448	6.06	−26.41	[9]
P159-02	6.38	−26.74	[9]
J1048-0109	6.68	−25.96	[9]
J1148+0702	6.34	−26.43	[9]
J1207+0630	6.04	−26.57	[9]
P183+05	6.44	−26.99	[9]
P217-16	6.15	−26.89	[9]
J1509-1749	6.12	−27.09	[9]
P231-20	6.59	−27.14	[9]
P308-21	6.23	−26.30	[9]
J2211-3206	6.34	−26.65	[9]
J2318-3113	6.44	−26.06	[9]
J2318-3029	6.15	−26.16	[9]
P359-06	6.17	−26.74	[9]
J0100+2802	6.33	−29.30	[10]
P338+29	6.66	−26.01	[14]
J0305-3150	6.61	−26.13	[15]

UV and X-ray observations: (i) less than 20 $z\sim6$ quasars fainter than $M_{\rm UV}=-23.75$ have been discovered so far (Matsuoka et al. 2018); (ii) none $z\sim6$ quasar with $L_{\rm X}<4\times10^{44}$ erg s^{-1} has been detected so far with Chandra (Vito et al. 2019a). Our predictions show that the SED of a faint AGN is instead well above ORIGINS' sensitivities at all wavelengths and also above the sensitivities of two SPICA's bands for all the simulations we performed. This result emphasizes the important role that future MIR facilities would have in studying the faint-end of the UV and X-ray luminosity function in $z\sim6$ AGN.

The *AGNcone* runs show that quasars with $M_{\rm UV}<-25$ are very easily detectable both by ORIGINS and SPICA at a signal-to-noise ratio high enough to get good-quality spectra even in these very distant sources. We notice that only ∼20 quasars have been detected so far with the *Spitzer* / *Herschel* telescopes at $z\gtrsim6$ (Leipski et al. 2014; Lyu, Rieke & Alberts 2016), and most of them (> 80 per cent) are bright ($M_{\rm UV}<-26$). Quasars fainter than $M_{\rm UV}=-26$ have been detected so far at mm wavelengths at $>5\sigma$ only in two $z\geq6$ quasars (J1048-0109 and P167-13 by Venemans et al. 2018).

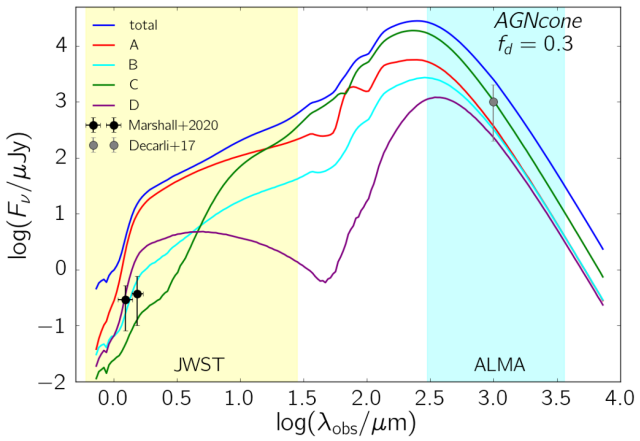

Figure 10. Comparison between the SEDs extracted from sources A, B, C, D in the field of view of the *AGNcone* run with $f_{\rm d}=0.3$, keeping the same colour legend as in Fig. 4. The total SED is instead plotted with a blue solid line. Black points indicate rest-frame UV limits from deep *HST* observations by Marshall et al. (2020), whereas the grey point FIR fluxes for star-forming companion galaxies around quasars from Decarli et al. (2017).

Our results show that the ORIGINS telescope will be an extremely powerful instrument for studying the properties of the most distant galaxies and quasars known so far.

5.1 Unveiling faint/obscured AGN

Combined ALMA data with follow-up *JWST* and /or[20] ORIGINS observations will be crucial to discover faint/obscured AGN and to distinguish them from galaxies without active nuclei. In fact, by comparing the predicted fluxes in ORIGINS band 1 and/or MIRI band at 29 μm ($F_{29\mu\rm m}$) with the ones in ALMA band 7 $F_{\rm band7}$, we find

$$\frac{F_{29\mu\rm m}(AGNsphere)/F_{\rm band7}(AGNsphere)}{F_{29\mu\rm m}(noAGN)/F_{\rm band7}(noAGN)}\approx 8-10,$$

meaning that we expect a a MIR-to-FIR excess of one order of magnitude in the case of a faint AGN host galaxy (*AGNsphere*) with respect to a star-forming galaxy without AGN (*noAGN*). This result shows that by following up with *JWST* and/or ORIGINS sources already detected with ALMA it will be possible to discriminate between star-forming galaxies and faint/obscured AGN.

We note that, given the limited resolution (∼200 pc) of the hydrodynamical simulations adopted in this work, we cannot resolve the torus (∼0.1–10 pc) that is, therefore, not included in our modelling. The presence of a dusty torus surrounding accreting BHs provides an additional source of MIR emission boosting the MIR excess expected in AGN. This can increase both the detectability of faint quasars with a SPICA-like telescope and the possibility of exploiting the synergy between ALMA and MIR facilities to unveil dust-obscured AGN. For example, we qualitatively show in Fig. 11 how our predicted SEDs would change with the inclusion of the emission from the dusty torus. For this comparison, we consider the *AGNsphere* case ($M_{\rm UV}=-23.4$), since we aim to investigate the ability of MIR

[20]The *James Webb Space Telescope* is planned to fly on 2021 October 31, with 10 yr of operation goal. The proposed ORIGINS mission is planned for launch in the early 2030s, so it will ideally continue the work of *JWST*.

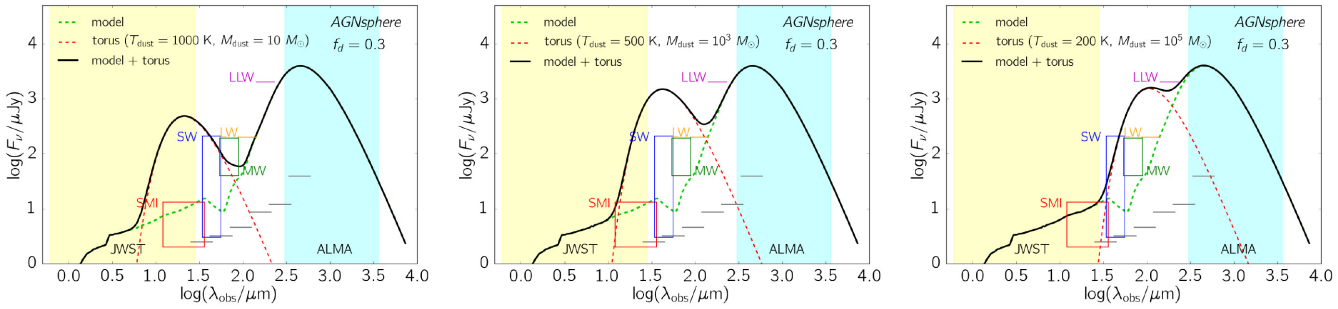

Figure 11. Predicted SEDs with the inclusion of the dusty torus emission to our models for the *AGNsphere* case with $f_d = 0.3$. The green dashed line refers to the original model, the red dashed line to the torus and the black solid line to the sum of the two. The torus emission is modelled as a greybody with M_{dust} and T_{dust} as specified in the panel, and $\beta_{dust} = 2$.

telescopes to unveil faint AGN. As a proof of concept, we simply model the torus emission as a single-temperature T_{dust} greybody, with dust mass M_{dust}, and $\beta_{dust} = 2$. We consider different models to cover the range in masses ($10^1 - 10^5$ $M_\odot$) and temperatures (200–1200 K) constrained by theoretical models (Schartmann et al. 2005; Stalevski et al. 2016) and observations (García-Burillo et al. 2016, 2019).

The MIR emission from the torus brings the SEDs of the faint AGN of our model easily within the reach of a SPICA-like telescope, for a wide range of the torus parameters considered. This further expands the potential of future MIR telescopes in the discovery and the study of faint AGN at high redshift.

We stress that this is a rough estimate that – among other things – neglects the torus geometry, i.e. the fact that UV emission is extinguished along the equatorial plane. Therefore, UV photons would escape only towards the polar regions, reducing the amount of dust on $\lesssim$200 pc scales directly irradiated by the AGN and possibly the IR emission coming from high temperature ($T_d \sim$ 200–300 K) regions. We plan to include the torus emission in a consistent way in our model in a future work and to further examine its impact on our results and on the potential of future facilities.

6 SUMMARY AND CONCLUSIONS

In this work, we have considered a suite of zoom-in cosmological hydrodynamic simulations of a massive halo ($\sim 10^{12}$ $M_\odot$) at $z \sim 6$ (B18). The set of simulations include a control simulation of a highly star-forming galaxy (SFR $\sim$600 $M_\odot$ yr^{-1}) without BHs (called *noAGN* run), and two simulations with accreting BHs that account for AGN kinetic feedback distributed according to a spherical (*AGNsphere* run) and bi-conical (*AGNcone* run) geometry. These two different feedback prescriptions result in different SFRs of the host galaxy ($\sim$300 and $\sim$200 $M_\odot$ yr^{-1} in *AGNsphere* and *AGNcone*, respectively), and AGN activity ($\sim$3 and $\sim$90 $M_\odot$ yr^{-1} in *AGNsphere* and *AGNcone*, respectively).

We performed dusty RT calculations of the three runs in post-process by exploiting the code SKIRT (Baes et al. 2003; Baes & Camps 2015; Camps & Baes 2015; Camps et al. 2016) with the aim of understanding the impact of radiative feedback on the observed SEDs of $z \sim 6$ galaxies. We have considered (i) intrinsic AGN SEDs defined by a composite power-law $F_\lambda \propto \lambda^\alpha$ constrained through observational and theoretical arguments; (ii) SMC dust properties (grain size distribution and composition); (iii) different total dust mass content (parametrized in terms of the dust-to-metal ratios f_d = 0.08 and 0.3), and we have explored how different assumptions affect the observational properties of galaxies in the EoR. By analyzing the synthetic emission maps and SEDs resulting from our calculations we have found the following results:

(i) In dusty galaxies ($M_d \gtrsim 3 \times 10^7$ $M_\odot$) a large fraction ($\gtrsim$50 per cent) of UV emission is obscured by dust.

(ii) Large UV luminosity variations with viewing angle, can be at least partially due to the inhomogeneous distribution of dusty gas on scales $\gtrsim$100 pc.

(iii) Simulations including AGN radiation show the presence of a clumpy, warm ($\approx$200–300 K) dust component, in addition to a colder ($\approx$50–70 K) and more diffuse dusty medium, heated by stars; warm dust provides up to 50 per cent of the total IR luminosity, though constituting only a small fraction ($\lesssim$0.1 per cent) of the overall mass content.

We have tested our model by comparing the simulated SEDs with observations of $z \sim 6$ bright ($M_{UV} \lesssim -26$) quasars, the only class of sources for which multiwavelength observations, ranging from the optical-NIR to the mm, are available so far. For what concerns the intrinsic SEDs, we have considered two variations for the rest-frame UV band: a fiducial value $\alpha_{UV}^{fid} = -1.7$ suggested by observations of unreddened quasars (Richards et al. 2003), and a steeper slope $\alpha_{UV}^{steep} = -2.3$ supported by observations of reddened quasars (Gallerani et al. 2010) and theoretical arguments (Shakura & Sunyaev 1973). The main findings of this comparison are the following:

(i) We find a good agreement between simulations and both MIR (*Spitzer*/*Herschel*) and millimetric (ALMA) data, in the case of $\alpha_{UV}^{fid} = -1.7$. In the rest-frame UV, our predicted SEDs are underluminous with respect to data, suggesting peculiar extinction properties (Gallerani et al. 2010, see also Di Mascia et al. in preparation).

(ii) The case $\alpha_{UV}^{steep} = -2.3$ cannot explain the *Spitzer*/IRAC flux at $\lambda_{obs} = 24$ μm and show a slope in the MIR that does not agree with *Spitzer*/IRS spectra. This discrepancy can be possibly alleviated by adding to our model the emission arising from a dusty torus with $T_d \sim$ 1500 K, close to sublimation temperature of graphite and silicate grains (Netzer 2015).

(iii) Quasars powered by SMBHs are part of complex, dust-rich merging systems, containing both multiple accreting BHs and star-forming galaxies that, because of strong dust absorption, are below the detection limit of current deep optical-NIR observations (Mechtley et al. 2012), but appear as SMG companions, consistently with recent shallow ALMA data Decarli et al. (2017). Deeper ALMA and future *JWST* observations are required to study the environment in which $z \sim 6$ quasars form and evolve.

Given the good agreement between our results and rest-frame MIR observations, we exploit our simulations to make predictions for the proposed OST (Wiedner et al. 2020), a possible selection to NASA's large strategic science missions, and for a MIR telescope with the same technical specifications of the SPICA (e.g. Spinoglio et al. 2017; Gruppioni et al. 2017; Egami et al. 2018; Roelfsema et al. 2018), an IR space mission, initially considered as a candidate for the M5 mission, but cancelled in October 2020 (Clements et al. 2020). We end up with the following conclusions:

(i) Highly star-forming galaxies (SFR $\sim 600\,\mathrm{M}_\odot\,\mathrm{yr}^{-1}$) without an active AGN will be easily detected by ORIGINS. It will also be able to probe the peak of the dust emission, allowing a solid estimate of the dust temperature in star-forming galaxies at high redshift. These galaxies would also be detected by a SPICA-like telescope, if lensed by a factor $\mu \gtrsim 5$.

(ii) Bright high-z quasars ($M_{\mathrm{UV}} < -26$) are detectable with ORIGINS/SPICA at an S/N ratio high enough to get high-quality spectra even in these very distant sources.

(iii) The FIR/MIR flux ratio in star-forming galaxies is one order of magnitude higher with respect to AGN hosts, even in the case of low accretion rates ($\dot{M}_{\mathrm{BH}} \sim 3\,\mathrm{M}_\odot\,\mathrm{yr}^{-1}$). By following up with ORIGINS/SPICA galaxies already detected with ALMA it will be possible to unveil faint and/or dust-obscured AGN, whose fraction is expected to be large (>85 per cent) at high redshift (e.g. Vito et al. 2014, 2018; see also Davies et al. 2019). Our FIR/MIR estimate is quite conservative, because our model does not include the emission from the dusty torus, which is expected to boost the MIR flux by up to two order of magnitudes in ORIGINS/SPICA bands.

These results highlight the importance of a new generation of MIR telescopes to understand the properties of dusty galaxies and AGN at the EoR.

ACKNOWLEDGEMENTS

FD thanks Alessandro Lupi, Laura Sommovigo and Milena Valentini for helpful discussions and Peter Camps for code support. We acknowledge fruitful discussions with Paola Andreani, Sarah Bosman, Eiichi Egami, Carlotta Gruppioni, Francesca Pozzi, Luigi Spinoglio, Christian Vignali. SG acknowledges support from the ASI-INAF n. 2018-31-HH.0 grant and PRIN-MIUR 2017 (PI Fabrizio Fiore). AF and SC acknowledge support from the ERC Advanced Grant INTERSTELLAR H2020/740120. Any dissemination of results must indicate that it reflects only the author's view and that the Commission is not responsible for any use that may be made of the information it contains. Generous support from the Carl Friedrich von Siemens-Forschungspreis der Alexander von Humboldt-Stiftung Research Award is kindly acknowledged (AF). We acknowledge usage of the PYTHON programming language (Van Rossum & de Boer 1991; Van Rossum & Drake 2009), ASTROPY (Astropy Collaboration et al. 2013), CYTHON (Behnel et al. 2011), MATPLOTLIB (Hunter 2007), NUMPY (van der Walt, Colbert & Varoquaux 2011), PYNBODY (Pontzen et al. 2013), and SCIPY (Virtanen et al. 2020).

DATA AVAILABILITY

Part of the data underlying this paper were accessed from the computational resources available to the Cosmology Group at Scuola Normale Superiore, Pisa (IT). The derived data generated in this research will be shared on reasonable request to the corresponding author.

REFERENCES

Allevato V. et al., 2016, ApJ, 832, 70
Aoyama S., Hou K. C., Shimizu I., Hirashita H., Todoroki K., Choi J. H., Nagamine K., 2017, MNRAS, 466, 105
Arata S., Yajima H., Nagamine K., Li Y., Khochfar S., 2019, MNRAS, 488, 2629
Asano R. S., Takeuchi T. T., Hirashita H., Inoue A. K., 2013a, Earth, Planets, and Space, 65, 213
Asano R. S., Takeuchi T. T., Hirashita H., Nozawa T., 2013b, MNRAS, 432, 637
Asplund M., Grevesse N., Sauval A. J., Scott P., 2009, ARA&A, 47, 481
Astropy Collaboration et al., 2013, A&A, 558, A33
Baes M., Camps P., 2015, Astron. Comput., 12, 33
Baes M. et al., 2003, MNRAS, 343, 1081
Bakx T. J. L. C. et al., 2020, MNRAS, 493, 4294
Barai P., Gallerani S., Pallottini A., Ferrara A., Marconi A., Cicone C., Maiolino R., Carniani S., 2018, MNRAS, 473, 4003 (B18)
Bañados E. et al., 2014, AJ, 148, 14
Bañados E. et al., 2018, Nature, 553, 473
Behnel S., Bradshaw R., Citro C., Dalcin L., Seljebotn D., Smith K., 2011, Comput. Sci. Eng., 13, 31
Behrens C., Pallottini A., Ferrara A., Gallerani S., Vallini L., 2018, MNRAS, 477, 552
Berta S. et al., 2013, A&A, 551, A100
Bertoldi F., Carilli C. L., Cox P., Fan X., Strauss M. A., Beelen A., Omont A., Zylka R., 2003a, A&A, 406, L55
Bertoldi F. et al., 2003b, A&A, 409, L47
Bianchi S., Schneider R., 2007, MNRAS, 378, 973
Blecha L., Snyder G. F., Satyapal S., Ellison S. L., 2018, MNRAS, 478, 3056
Bondi H., 1952, MNRAS, 112, 195
Bondi H., Hoyle F., 1944, MNRAS, 104, 273
Bongiorno A. et al., 2012, MNRAS, 427, 3103
Booth C. M., Schaye J., 2009, MNRAS, 398, 53
Bruzual G., Charlot S., 2003, MNRAS, 344, 1000
Camps P., Baes M., 2015, Astron. Comput., 9, 20
Camps P., Trayford J. W., Baes M., Theuns T., Schaller M., Schaye J., 2016, MNRAS, 462, 1057
Carilli C. L., Walter F., 2013, ARA&A, 51, 105
Carnall A. C. et al., 2015, MNRAS, 451, L16
Carniani S. et al., 2016, A&A, 591, A28
Carniani S. et al., 2019, MNRAS, 489, 3939
Chabrier G., 2003, Publ. Astron. Soc. Aust., 115, 763
Chakrabarti S., Cox T. J., Hernquist L., Hopkins P. F., Robertson B., Di Matteo T., 2007, ApJ, 658, 840
Chakrabarti S., Whitney B. A., 2009, ApJ, 690, 1432
Cicone C. et al., 2015, A&A, 574, A14
Clements D. L., Serjeant S., Jin S., 2020, Nature, 587, 548
Connor T. et al., 2019, ApJ, 887, 171
Connor T. et al., 2020, ApJ, 900, 189
Cowie L. L., Barger A. J., Bauer F. E., González-López J., 2020, ApJ, 891, 69
Cresci G. et al., 2015a, A&A, 582, A63
Cresci G. et al., 2015b, ApJ, 799, 82
Dalla Vecchia C., Schaye J., 2008, MNRAS, 387, 1431
Davies F. B., Hennawi J. F., Eilers A. C., 2019, ApJ, 884, L19
Decarli R. et al., 2017, Nature, 545, 457
De Young D. S., 1989, ApJ, 342, L59
Di Matteo T., Springel V., Hernquist L., 2005, Nature, 433, 604
Draine B. T., 2003a, ARA&A, 41, 241
Draine B. T., 2003b, ApJ, 598, 1017
Draine B. T., 2003c, ApJ, 598, 1026
Draine B. T., Salpeter E. E., 1979, ApJ, 231, 77
Draine B. T. et al., 2007, ApJ, 663, 866
Dubois Y., Devriendt J., Slyz A., Teyssier R., 2010, MNRAS, 409, 985
Dubois Y., Gavazzi R., Peirani S., Silk J., 2013, MNRAS, 433, 3297
Egami E. et al., 2018, Publ. Astron. Soc. Aust., 35, 48
Fabian A. C., 1999, MNRAS, 308, L39

Fan X. et al., 2000, AJ, 120, 1167
Fan X. et al., 2006, AJ, 131, 1203
Ferrara A., Salvadori S., Yue B., Schleicher D., 2014, MNRAS, 443, 2410
Ferrara A., Viti S., Ceccarelli C., 2016, MNRAS, 463, L112
Fiore F., Elvis M., McDowell J. C., Siemiginowska A., Wilkes B. J., 1994, ApJ, 431, 515
Gallerani S., Fan X., Maiolino R., Pacucci F., 2017a, Publ. Astron. Soc. Aust., 34, e022
Gallerani S., Ferrara A., Neri R., Maiolino R., 2014, MNRAS, 445, 2848
Gallerani S. et al., 2010, A&A, 523, A85
Gallerani S. et al., 2017b, MNRAS, 467, 3590
García-Burillo S. et al., 2016, ApJ, 823, L12
García-Burillo S. et al., 2019, A&A, 632, A61
Gilli R. et al., 2014, A&A, 562, A67
Groves B., Dopita M. A., Sutherland R. S., Kewley L. J., Fischera J., Leitherer C., Brandl B., van Breugel W., 2008, ApJS, 176, 438
Gruppioni C. et al., 2016, MNRAS, 458, 4297
Gruppioni C. et al., 2017, Publ. Astron. Soc. Aust., 34, e055
Hahn O., Abel T., 2011, MNRAS, 415, 2101
Haiman Z., 2013, in Wiklind T., Mobasher B., Bromm V., eds, The First Galaxies, Vol. 396, Astrophysics and Space Science Library. Springer-Verlag, Berlin, p. 293
Hernán-Caballero A., Hatziminaoglou E., 2011, MNRAS, 414, 500
Hickox R. C., Alexander D. M., 2018, ARA&A, 56, 625
Hirashita H., Aoyama S., 2019, MNRAS, 482, 2555
Hirashita H., Nozawa T., Villaume A., Srinivasan S., 2015, MNRAS, 454, 1620
Hjorth J., Vreeswijk P. M., Gall C., Watson D., 2013, ApJ, 768, 173
Hopkins P. F., Richards G. T., Hernquist L., 2007, ApJ, 654, 731
Hoyle F., Lyttleton R. A., 1939, Proc. Camb. Phil. Soc., 35, 405
Hunter J. D., 2007, Comput. Sci. Eng., 9, 90
Jiang L., Fan X., Vestergaard M., Kurk J. D., Walter F., Kelly B. C., Strauss M. A., 2007, AJ, 134, 1150
Jiang L. et al., 2009, AJ, 138, 305
Jiang L. et al., 2016, ApJ, 833, 222
Jonsson P., Groves B. A., Cox T. J., 2010, MNRAS, 403, 17
Juarez Y., Maiolino R., Mujica R., Pedani M., Marinoni S., Nagao T., Marconi A., Oliva E., 2009, A&A, 494, L25
Kashikawa N. et al., 2015, ApJ, 798, 28
Kormendy J., Ho L. C., 2013, ARA&A, 51, 511
Kormendy J., Richstone D., 1995, ARA&A, 33, 581
Koss M., Mushotzky R., Treister E., Veilleux S., Vasudevan R., Trippe M., 2012, ApJ, 746, L22
Kroupa P., 2002, Science, 295, 82
Kulkarni G., Worseck G., Hennawi J. F., 2019, MNRAS, 488, 1035
Kurk J. D. et al., 2007, ApJ, 669, 32
Laporte N. et al., 2017, ApJ, 837, L21
Latif M. A., Ferrara A., 2016, Publ. Astron. Soc. Aust., 33, e051
Latif M. A., Schleicher D. R. G., Schmidt W., Niemeyer J., 2013, MNRAS, 433, 1607
Leipski C. et al., 2013, ApJ, 772, 103
Leipski C. et al., 2014, ApJ, 785, 154
Leitherer C. et al., 1999, ApJS, 123, 3
Liang L., Feldmann R., Hayward C. C., Narayanan D., Çatmabacak O., Keres D., Faucher-Giguére C. A., Hopkins P. F., 2021, MNRAS, 502, 3210
Liang L. et al., 2019, MNRAS, 489, 1397
Li J. et al., 2020, ApJ, 889, 162
Li Y. et al., 2008, ApJ, 678, 41
Lupi A., Haardt F., Dotti M., Fiacconi D., Mayer L., Madau P., 2016, MNRAS, 456, 2993
Lusso E., Worseck G., Hennawi J. F., Prochaska J. X., Vignali C., Stern J., O'Meara J. M., 2015, MNRAS, 449, 4204
Lyu J., Rieke G. H., Alberts S., 2016, ApJ, 816, 85
Magorrian J. et al., 1998, AJ, 115, 2285
Maiolino R., Schneider R., Oliva E., Bianchi S., Ferrara A., Mannucci F., Pedani M., Roca Sogorb M., 2004, Nature, 431, 533
Maiolino R. et al., 2005, A&A, 440, L51
Maiolino R. et al., 2012, MNRAS, 425, L66
Manti S., Gallerani S., Ferrara A., Feruglio C., Graziani L., Bernardi G., 2016, MNRAS, 456, 98
Marconi A., Risaliti G., Gilli R., Hunt L. K., Maiolino R., Salvati M., 2004, MNRAS, 351, 169
Marshall M. A. et al., 2020, ApJ, 900, 21
Matsuoka Y. et al., 2016, ApJ, 828, 26
Matsuoka Y. et al., 2018, ApJ, 869, 150
Ma X. et al., 2019, MNRAS, 487, 1844
Mazzucchelli C. et al., 2017, ApJ, 849, 91
McGreer I. D., Fan X., Jiang L., Cai Z., 2018, AJ, 155, 131
Mechtley M. et al., 2012, ApJ, 756, L38
Mortlock D. J. et al., 2011, Nature, 474, 616
Murray N., Quataert E., Thompson T. A., 2005, ApJ, 618, 569
Nanni R., Vignali C., Gilli R., Moretti A., Brand t W. N., 2017, A&A, 603, A128
Nenkova M., Sirocky M. M., Ivezić Z., Elitzur M., 2008, ApJ, 685, 147
Netzer H., 2015, ARA&A, 53, 365
Novak M. et al., 2019, ApJ, 881, 63
Nozawa T., Asano R. S., Hirashita H., Takeuchi T. T., 2015, MNRAS, 447, L16
Ono Y. et al., 2018, Publ. Astron. Soc. Japan, 70, S10
Orofino M. C., Ferrara A., Gallerani S., 2021, MNRAS, 502, 2757
Pacucci F., Ferrara A., Grazian A., Fiore F., Giallongo E., Puccetti S., 2016, MNRAS, 459, 1432
Pacucci F., Volonteri M., Ferrara A., 2015, MNRAS, 452, 1922
Padoan P., Federrath C., Chabrier G., Evans N. J. I., Johnstone D., Jørgensen J. K., McKee C. F., Nordlund A., 2014, in Henrik B., Ralf S. K., Cornelis P. D., Thomas H., eds, Protostars and Planets VI. University of Arizona Press, Tucson, AZ, p. 77
Padoan P., Nordlund a., 2011, ApJ, 730, 40
Pallottini A., Ferrara A., Bovino S., Vallini L., Gallerani S., Maiolino R., Salvadori S., 2017, MNRAS, 471, 4128
Pezzulli E., Valiante R., Orofino M. C., Schneider R., Gallerani S., Sbarrato T., 2017, MNRAS, 466, 2131
Piconcelli E., Jimenez-Bailón E., Guainazzi M., Schartel N., Rodríguez-Pascual P. M., Santos-Lleó M., 2005, A&A, 432, 15
Pilbratt G. L. et al., 2010, A&A, 518, L1
Planck Collaboration XIII, 2016, A&A, 594, A13
Pontzen A., Rovskar R., Stinson G. S., Woods R., Reed D. M., Coles J., Quinn T. R., 2013, pynbody: Astrophysics Simulation Analysis for Python, Astrophysics Source Code Library, record ascl:1305.002
Pozzi F. et al., 2012, MNRAS, 423, 1909
Pringle J. E., 1981, ARA&A, 19, 137
Reed S. L. et al., 2015, MNRAS, 454, 3952
Ricci C. et al., 2017, Nature, 549, 488
Richards G. T. et al., 2003, AJ, 126, 1131
Riechers D. A. et al., 2009, ApJ, 703, 1338
Roebuck E., Sajina A., Hayward C. C., Pope A., Kirkpatrick A., Hernquist L., Yan L., 2016, ApJ, 833, 60
Roelfsema P. R. et al., 2018, Publ. Astron. Soc. Aust., 35, e030
Sazonov S. Y., Ostriker J. P., Sunyaev R. A., 2004, MNRAS, 347, 144
Schartmann M., Meisenheimer K., Camenzind M., Wolf S., Henning T., 2005, A&A, 437, 861
Schawinski K. et al., 2006, Nature, 442, 888
Schaye J. et al., 2015, MNRAS, 446, 521
Schleicher D. R. G., Palla F., Ferrara A., Galli D., Latif M., 2013, A&A, 558, A59
Schneider R., Bianchi S., Valiante R., Risaliti G., Salvadori S., 2015, A&A, 579, A60
Shakura N. I., Sunyaev R. A., 1973, A&A, 500, 33
Shang C., Bryan G. L., Haiman Z., 2010, MNRAS, 402, 1249
Shen X., Hopkins P. F., Faucher-Giguère C. A., Alexander D. M., Richards G. T., Ross N. P., Hickox R. C., 2020, MNRAS, 495, 3252
Sijacki D., Springel V., Di Matteo T., Hernquist L., 2007, MNRAS, 380, 877
Silk J., 2005, MNRAS, 364, 1337
Silverman J. D. et al., 2020, ApJ, 899, 154
Snyder G. F., Hayward C. C., Sajina A., Jonsson P., Cox T. J., Hernquist L., Hopkins P. F., Yan L., 2013, ApJ, 768, 168

Sommovigo L., Ferrara A., Pallottini A., Carniani S., Gallerani S., Decataldo D., 2020, MNRAS, 497, 956
Spinoglio L. et al., 2017, Publ. Astron. Soc. Aust, 34, e057
Springel V., 2005, MNRAS, 364, 1105
Springel V., Di Matteo T., Hernquist L., 2005, MNRAS, 361, 776
Springel V., Hernquist L., 2003, MNRAS, 339, 289
Stalevski M., Fritz J., Baes M., Nakos T., Popović L. C., 2012, MNRAS, 420, 2756
Stalevski M., Ricci C., Ueda Y., Lira P., Fritz J., Baes M., 2016, MNRAS, 458, 2288
Stefan I. I. et al., 2015, MNRAS, 451, 1713
Stratta G., Gallerani S., Maiolino R., 2011, A&A, 532, A45
Tanaka T., Haiman Z., 2009, ApJ, 696, 1798
Tazaki R., Ichikawa K., 2020, ApJ, 892, 149
Tazaki R., Ichikawa K., Kokubo M., 2020, ApJ, 892, 84
Teyssier R., Moore B., Martizzi D., Dubois Y., Mayer L., 2011, MNRAS, 414, 195
Tielens A. G. G. M., McKee C. F., Seab C. G., Hollenbach D. J., 1994, ApJ, 431, 321
Todini P., Ferrara A., 2001, MNRAS, 325, 726
Tornatore L., Borgani S., Dolag K., Matteucci F., 2007, MNRAS, 382, 1050
Trayford J. W. et al., 2017, MNRAS, 470, 771
Urry C. M., Padovani P., 1995, Publ. Astron. Soc. Pac., 107, 803
Valiante R., Schneider R., Bianchi S., Andersen A. C., 2009, MNRAS, 397, 1661
Vallini L., Ferrara A., Pallottini A., Gallerani S., 2017, MNRAS, 467, 1300
Vanden Berk D. E. et al., 2001, ApJ, 122, 549–564
van der Walt S., Colbert S. C., Varoquaux G., 2011, Comput. Sci. Eng., 13, 22
Van Rossum G., de Boer J., 1991, CWI Q., 4, 283
Van Rossum G., Drake F. L., 2009, Python 3 Reference Manual. CreateSpace, Scotts Valley, CA
Venanzi M., Hönig S., Williamson D., 2020, ApJ, 900, 174
Venemans B. P., McMahon R. G., Warren S. J., Gonzalez-Solares E. A., Hewett P. C., Mortlock D. J., Dye S., Sharp R. G., 2007, MNRAS, 376, L76
Venemans B. P., Walter F., Zschaechner L., Decarli R., De Rosa G., Findlay J. R., McMahon R. G., Sutherland W. J., 2016, ApJ, 816, 37
Venemans B. P. et al., 2012, ApJ, 751, L25
Venemans B. P. et al., 2013, ApJ, 779, 24
Venemans B. P. et al., 2015, MNRAS, 453, 2259
Venemans B. P. et al., 2017a, ApJ, 845, 154
Venemans B. P. et al., 2017b, ApJ, 851, L8
Venemans B. P. et al., 2018, ApJ, 866, 159
Vignali C. et al., 2018, MNRAS, 477, 780
Virtanen P. et al., 2020, Nat. Methods, 17, 261
Vito F., Gilli R., Vignali C., Comastri A., Brusa M., Cappelluti N., Iwasawa K., 2014, MNRAS, 445, 3557
Vito F. et al., 2018, MNRAS, 473, 2378
Vito F. et al., 2019a, A&A, 630, A118
Vito F. et al., 2019b, A&A, 628, L6
Volonteri M., Haardt F., Madau P., 2003, ApJ, 582, 559
Wada K., Schartmann M., Meijerink R., 2016, ApJ, 828, L19
Walter F., Riechers D., Cox P., Neri R., Carilli C., Bertoldi F., Weiss A., Maiolino R., 2009, Nature, 457, 699
Walter F. et al., 2003, Nature, 424, 406
Wang F. et al., 2018, ApJ, 869, L9
Wang F. et al., 2019, ApJ, 884, 30
Wang F. et al., 2021, ApJ, 907, L1
Wang R. et al., 2013, ApJ, 773, 44
Wang R. et al., 2016, ApJ, 830, 53
Weinberger R. et al., 2018, MNRAS, 479, 4056
Weingartner J. C., Draine B. T., 2001, ApJ, 548, 296
Werner M. W. et al., 2004, ApJS, 154, 1
Wiedner M. C. et al., 2020, preprint (arXiv:2012.02731)
Wiersma R. P. C., Schaye J., Smith B. D., 2009, MNRAS, 393, 99
Willott C. J., Bergeron J., Omont A., 2017, ApJ, 850, 108
Willott C. J., McLure R. J., Jarvis M. J., 2003, ApJ, 587, L15
Willott C. J. et al., 2007, AJ, 134, 2435
Willott C. J. et al., 2010, AJ, 139, 906
Wiseman P., Schady P., Bolmer J., Krühler T., Yates R. M., Greiner J., Fynbo J. P. U., 2017, A&A, 599, A24
Wu X. B. et al., 2015, Nature, 518, 512
Wyithe J. S. B., Bolton J. S., 2011, MNRAS, 412, 1926
Xue Y. Q. et al., 2011, ApJS, 195, 10
Xu J., Sun M., Xue Y., 2020, ApJ, 894, 21
Younger J. D., Hayward C. C., Narayanan D., Cox T. J., Hernquist L., Jonsson P., 2009, MNRAS, 396, L66
Zafar T., Watson D., Fynbo J. P. U., Malesani D., Jakobsson P., de Ugarte Postigo A., 2011, A&A, 532, A143
Zafar T. et al., 2018, MNRAS, 480, 108
Zinn P. C., Middelberg E., Norris R. P., Dettmar R. J., 2013, ApJ, 774, 66
Zubovas K., Nayakshin S., King A., Wilkinson M., 2013, MNRAS, 433, 3079

APPENDIX A: CONVERGENCE OF THE DUST GRID

The dust content derived from the hydrodynamical simulations is distributed in an octree grid with a maximum of eight level of refinement, achieving a maximum resolution of ∼234 pc, as described in Section 2.2.2. This spatial resolution is comparable with the resolution of the hydrodynamical simulations, i.e. ∼200 pc at $z = 6$. In this section, we check if the number of refinement levels adopted in our fiducial setup is sufficient to achieve converge of the results. We perform three control simulations, in which the maximum refinement levels are 6, 7, and 9, corresponding to a spatial resolution of 937, 469, and 117 pc, respectively. In Fig. A1, we show the SED plot for the *AGNcone* run, adopting $f_{\rm d} = 0.08$ and the fiducial AGN SED, for the aforementioned values of the maximum refinement levels. The four SEDs mainly differ in the MIR range (6−15 μm rest frame). The MIR emission increases when increasing the number of refinement levels, because dust around AGN, which is heated to the highest temperatures, is better resolved. However, the variation between our fiducial model and the model at the highest resolution is less than 30 per cent in the MIR band, thus we conclude that the spatial resolution of the dust grid adopted in our calculations is sufficient to achieve reasonable numerical convergence.

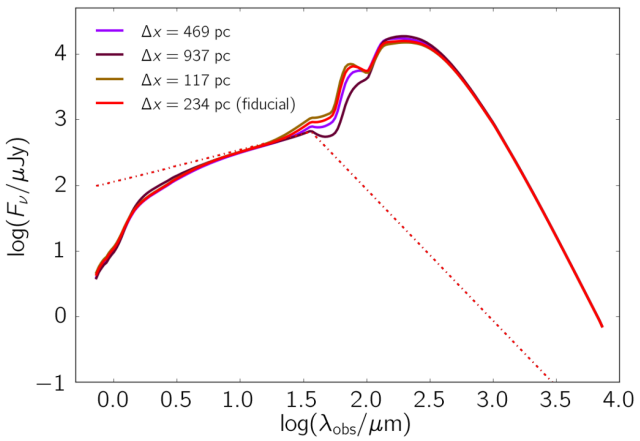

Figure A1. SED of the *AGNcone* run ($f_{\rm d} = 0.08$, fiducial AGN SED) for different numbers of the maximum refinement levels: 6, 7, 8 (fiducial) and 9, corresponding to 937, 469, 234 (fiducial) and 117 pc, respectively.

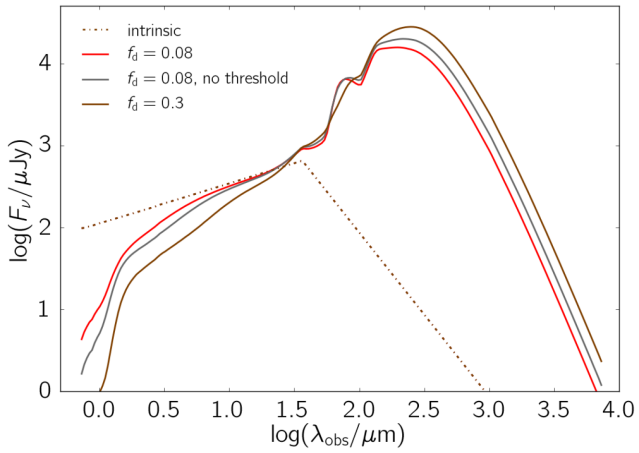

Figure B1. Comparison of the SEDs of the *AGNcone* run, assuming $f_d = 0.08$ (red), $f_d = 0.3$ (brown), and $f_d = 0.08$ without dust sputtering (grey).

APPENDIX B: DUST THERMAL SPUTTERING

We have assumed that dust grains with temperature above a given threshold ($T > 10^6$ K) are destroyed by thermal sputtering (Draine & Salpeter 1979; Tielens et al. 1994; Hirashita et al. 2015), as commonly done in simulations (Liang et al. 2019; Ma et al. 2019). However, this dust destruction process may be inefficient in the proximity of AGN, because of grain charging (Tazaki & Ichikawa 2020; Tazaki, Ichikawa & Kokubo 2020). To quantify how this assumption affects our results, we re-run the *AGNcone* model with the lower dust content, i.e. $f_d = 0.08$ (fifth row in Table 4), after removing the threshold on the dust temperature. In this case, the mass of emitting dust is a factor of ∼2 higher with respect to the fiducial run ($M_d = 6 \times 10^7$ M$_\odot$). In Fig. B1, we compare the SEDs obtained with $f_d = 0.08$ and 0.3 (red and brown lines, respectively) with the model in which dust sputtering is ignored (grey line). The higher dust mass in the model without dust sputtering increases both the attenuation in the UV and the re-emission in the FIR. The resulting SED lies between the $f_d = 0.08$ and 0.3 model results, underlining that the temperature threshold adopted does not affect significantly the main results of our work.

APPENDIX C: $\dot{M}_{BH}$–M_{UV} RELATION

For a radiation efficiency $\epsilon_r = 0.1$, the bolometric luminosity L_{bol} can be related to the BH accretion rate as follows:

$$L_{bol} \approx 1.5 \times 10^{12} \left(\frac{\dot{M}_{BH}}{\mathrm{M}_\odot\ \mathrm{yr}^{-1}} \right) L_\odot. \quad \text{(C1)}$$

Using the bolometric corrections reported in Table 3, we can convert the accretion rate into an UV luminosity by multiplying the bolometric luminosity by a factor[21] $f_{UV} = L_{UV}/L_{bol}$. Then, we adopt the definition of the AB magnitude

$$m_{AB} = -2.5 \log F_\nu - 48.6,$$

where F_ν is in cgs units, and we express M_{UV} in terms of the product λL_λ:

$$M_{UV} = 89.9 - 2.5 \log \left(\frac{\lambda L_\lambda}{\mathrm{erg\ s}^{-1}} \right), \quad \text{(C2)}$$

[21] In the case of the fiducial SED, $f_{UV} \approx 0.29$. The results are however very similar in the case of the UV-steep SED.

where[22] ν and λL_λ are evaluated at $\lambda = 1450$ Å. By combining the previous equations, we obtain

$$M_{UV} = -23.1 - 2.5 \log_{10} \left(\frac{\dot{M}_{BH}}{\mathrm{M}_\odot\ \mathrm{yr}^{-1}} \right). \quad \text{(C3)}$$

[22] In this expression, we do not include *k*-corrections for the distance modulus (μ) calculations. At $z = 6.3$, the difference between μ and the k-corrected one μ_k is $\mu = \mu_k + 2.1$.

This paper has been typeset from a TEX/LATEX file prepared by the author.